DEVELOPMENT OF MAGNETIC AND IMAGE BASED CELL CYTOMETRY TECHNIQUES

A Thesis Submitted to
the Graduate School of Engineering and Sciences of
İzmir Institute of Technology
in Partial Fulfillment of the Requirements for the Degree of

MASTER OF SCIENCE

in Bioengineering

by
Şeyda KELEŞ

June 2024
İZMİR

We approve the thesis of **Şeyda KELEŞ**

Examining Committee Members:

Assoc. Prof. Dr. Hüseyin Cumhur TEKİN

Department of Bioengineering, İzmir Institute of Technology

Prof. Dr. Engin ÖZÇİVİCİ

Department of Bioengineering, İzmir Institute of Technology

Assoc. Prof. Dr. Sinan GÜVEN

Department of Medical Biology, Dokuz Eylül University

16 July 2024

Assoc. Prof. Dr. Hüseyin Cumhur TEKİN

Supervisor, Department of Bioengineering, İzmir Institute of Technology

Assoc. Prof. Dr. Ceyda ÖKSEL KARAKUŞ

Head of the Department of Bioengineering

Prof. Dr. Mehtap EANES

Dean of the Graduate School of Engineering and Science

ACKNOWLEDGMENTS

First and foremost, I would like to express my gratitude to my advisor, Assoc. Prof. Dr. Hüseyin Cumhur TEKİN, for his guidance, encouragement, and extensive knowledge provided throughout my master's thesis research over 3 years.

I would like to thank everyone at the Biomedical Micro and Nano Systems Laboratory (LBMS) for their hard work. I am also grateful to the Izmir Institute of Technology's Bioengineering Department faculty members for sharing their expertise and knowledge with me during my master's program.

I wish to acknowledge the financial support provided by the Scientific and Technical Council of Turkey (grant number: 22AG032), the Izmir Institute of Technology Research Fund (grant number: 2023IYTE50-BAP), and the support of The Scientific and Technological Research Council of Turkey for the 2210-C BIDEB graduate scholarship.

Lastly, I extend my deepest love and gratitude to my dear mother, father, and sister, who have always been by my side and supported me with their love.

ABSTRACT

DEVELOPMENT OF MAGNETIC AND IMAGE BASED CELL CYTOMETRY TECHNIQUES

Flow cytometry allows for the measurement of cells or single-cell properties using various parameters. In this thesis, a novel image-based cytometry approach was developed for measuring the density of microparticles under flow conditions within a microfluidic chip utilizing magnetic levitation and deep learning analysis. This method facilitates the differentiation of microparticles according to their densities without the necessity of labeling. Utilizing the You Only Look Once (YOLO) algorithm, a method was established to automatically and accurately analyze particle radius and levitation heights. Furthermore, microparticles with two different densities were successfully separated based on their densities. Subsequently, live and dead human monocyte cells (U-937) were analyzed. Thus, the developed image-based cytometry method facilitates the automatic analysis of microparticles, and cells based on their densities and radii. This approach will enable the real-time, label-free identification of various microparticle populations for different applications. Additionally, studies were conducted on microvalves to enable the use of this system for sorting purposes under flow conditions. In this context, the fabrication of micropneumatic valves was explored. Pneumatic valves created with polydimethylsiloxane (PDMS) membrane structures provide robust operation and fast fluidic manipulation. Pneumatic valve structures were fabricated quickly and simply using a 3D printed mold. Moreover, these valves could be closed at very low pressures and were shown to be usable in the magnetic levitation setup. Hence, new magnetic levitation-based cytometry applications can be conducted in future studies with the presented technique.

ÖZET

MANYETİK VE GÖRÜNTÜ TABANLI HÜCRE SİTOMETRİ TEKNİKLERİNİN GELİŞTİRİLMESİ

Akış sitometrisi çeşitli parametreler kullanılarak hücrelerin veya tek hücre özelliklerinin ölçülmesine olanak tanır. Bu tezde etiketlemeye gerek kalmadan hücrelerin veya mikropartiküllerin farklı yoğunluklarına göre ayrıştırılmasına olanak tanıyan manyetik levitasyon yöntemi kullanılmıştır. Ayrıca mikroakışkan çip içindeki mikropartiküllerin ve hücrelerin akış koşulları altında yoğunluğunu ölçen derin öğrenme tabanlı yeni bir görüntü sitometri tekniği üstünde çalışılmıştır. Bu bağlamda You Only Look Once (YOLO) algoritmasını kullanılarak parçacık yarıçapının ve levitayon yüksekliklerinin otomatik ve doğru analizini sağlayan bir yöntem geliştirilmiştir. Bununla birlikte farklı iki yoğunluğa sahip mikroparçacıklar birbirinden başarılı şekilde yoğunluklarına göre ayrıştırılmıştır. Devamında aynı şekilde insan monosit hücresinin (U-937) ölü ve canlı analizi yapılmıştır. Böylece, geliştirilen görüntü tabanlı sitometri yöntemi, mikropartiküllerin ve hücrelerin yoğunluklarına ve yarıçaplarına göre otomatik analizini kolaylaştırmıştır. Bu yaklaşım farklı uygulamalar için mikropartikül/hücre popülasyonlarının gerçek zamanlı, etiketsiz tanımlanmasına imkan tanıyabilecektir. Ayrıca bu sistemin akış altında ayrıştırma amacı ile kullanılabilmesi için mikrovalfler üzerinde çalışmalar gerçekleştirilmiştir. Bu kapsamda mikro pnömatik valf üretimi üzerinde çalışılmıştır. Polidimetilsiloksan (PDMS) membran yapıları ile oluşturulan pnömatik valfler, sağlam işleyişleri sayesinde hızlı akış manipülasyonuna olanak tanımaktadır. 3B baskı yöntemi ile üretilen kalıplar kullanılarak pnömatik valf yapıları hızlı ve basit bir şekilde üretilmiştir. Ayrıca, bu valfler çok düşük basınçlarda kapatılabilir ve manyetik levitasyon kurulumunda kullanılabilir olduğu gösterilmiştir. Bu nedenle, sunulan teknikle gelecekteki çalışmalarda yeni manyetik levitasyon tabanlı sitometri uygulamaları yürütülebilir.

TABLE OF CONTENTS

APPENDICES

LIST OF FIGURES

Figure **Page**

LIST OF ABBREVIATIONS

AI	artificial intelligence
ML	machine learning
DL	deep learning
CV	compute vision
CNN	convolutional neural network
FC	fully connected
YOLO	you only look once
IoU	intersection over union
AP	average precision
mAP	mean average precision
PDMS	polydimethylsiloxane
SL	stereolithography
MagLev	magnetic levitation
TP	true positive
FN	false negative
FP	false positive
TN	true negative
IIFC	intelligent imaging flow cytometer

CHAPTER 1

INTRODUCTION

In this chapter, cell separation methods are discussed. The image-based magnetic levitation method is explained, and its application in cell separation is illustrated with examples. Subsequently, the contributions of cytometry techniques combined with microfluidic-based systems are described. Finally, the aim of the thesis is explained.

1.1. Conventional Flow Cytometry Methods

The technique known as flow cytometry allows for the measurement of cells and their characteristics using a variety of parameters.[1] Unlike many other techniques, flow cytometry quantitatively examines the characteristics of individual cells within a diverse population.[2]

1.1.1. Optic Flow Cytometry

The fluidic system, computer, electronics, illumination source, and optical bench are the essential parts of an optic flow cytometer (Figure 1.1). Stained cells are probed by light sources as they move through the fluidic system in a single file. The optical system directs the light signals to photodetectors, which convert these signals into electronic signals that are stored and analyzed. The fluidic system ensures a stable, centrally focused single-file flow of cells using isotonic sheath fluid. Consequently, the emission signals generated from the cells reflect biological differences among them.[3]

Light scattering and fluorescence emission from a source of excitation, usually a laser beam striking in-motion particles is the fundamental idea behind flow cytometry. The information gathered from this process can be very helpful in understanding the molecular, biochemical, and physical characteristics of the particles. Light scattering has a direct correlation with the cell's morphological and structural characteristics. The number of fluorescent probes that are in place on the cell or cellular component determines the amount of fluorescence emission.[4]

The most crucial and time-consuming part of the manual analysis is finding homogenous cell populations within the data, when numerous populations are found within individual samples and sample comparisons take a long time. In addition, computational tools frequently must analyze large data sets.[5]

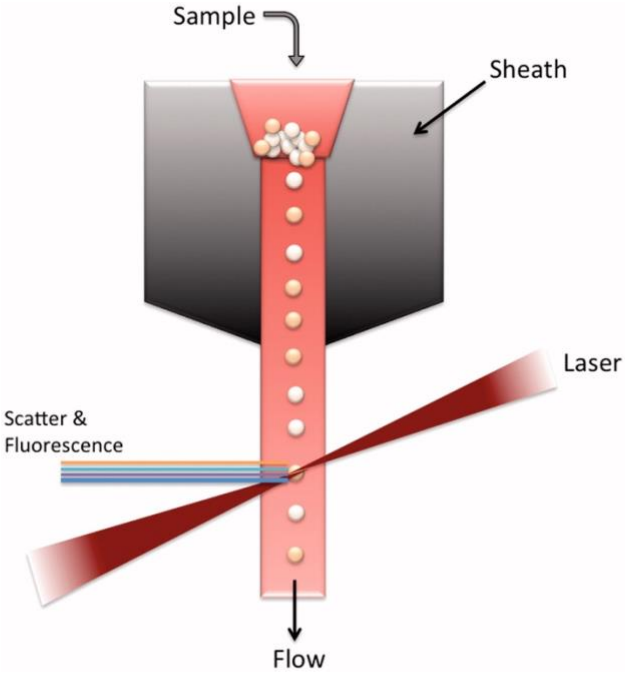

Figure 1.1. Illustration of optical flow cytometry.[3]

It is dependent upon particular magnetic or fluorescent indicators on the targeted cell's surface. Even though labeling is frequently a costly, time-consuming, and complex process, it can harm the sample being examined. Despite the content-rich, high-throughput screening that label-dependent strategies offer, this could impede their widespread adoption in clinical settings.[6] On the other hand, using multiple fluorophores to label distinct cell structures at the same time may cause emission spectra to overlap and necessitate the use of a compensation procedure. When examining rare cells like circulating tumor cells, this step is essential.[7] These drawbacks highlight the necessity of label-free, non-intrusive physical feature-based classification techniques.

1.1.2. Impedance-Based Flow Cytometry

An essential component of flow cytometry analysis is particle counting. The Coulter chamber was used for particle counting, one of the first applications of electrical analysis.[8] The foundation of the Coulter principle is the idea that a particle's electrical impedance differs from the flow gap in the flow channel. A 'sensing zone' is formed when a gap is positioned between the electrodes, altering the electrical current as it passes through the particle (Figure 1.2). The analysis of cell size about particle size and volume is based on this change in impedance. Additionally, many physical characteristics of the particle, including its size, shape, and orientation, affect the impedance change at the aperture.[9,10]

Beyond Coulter measurement, impedance-based cell characterization is possible. To characterize cells, impedance systems have been developed. It seems that impedance analysis holds the most potential for smaller devices and a wider variety of uses, however, there is always potential for improvement.[11]

The dielectric properties of cells allow for characterization without the need for immunological markers, which are costly, brittle, and have a limited shelf life.[12] Membrane morphology and function are reflected in dielectric properties like capacitance and conductance; these attributes are linked to physiological variations amongst cells or pathological alterations that develop in cells over time.[13]

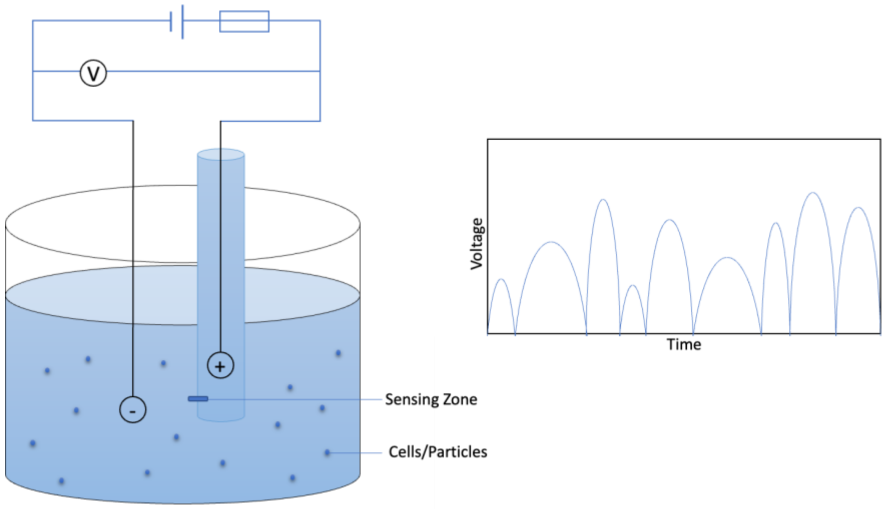

Figure 1.2. Illustration of Coulter Principle.

1.1.3. Image-Based Flow Cytometry

Imaging flow cytometry systems, which combine the advantages of microscope imaging with the statistical power of traditional flow cytometry to provide bright-field and fluorescence images,[14] can be complemented by magnetic levitation—a label-free, sensitive, and precise image-based detection technique that measures the density of particles exposed to a magnetic field while suspended in a paramagnetic environment.[15] Two opposing forces act on a diamagnetic object suspended in a paramagnetic medium and exposed to a magnetic field.[16] Due to the microparticles' relative density, it has two forces: a magnetic force from its sensitivity to the surroundings and suspension medium, and a buoyant force from the object itself. The object will stay suspended in the air at a height proportionate to its density in the equilibrium between these two forces.[17] The paramagnetic medium facilitates the levitation of objects by exerting a magnetic force that is proportionate to the variation in the medium's and the microparticle's magnetic susceptibility, in addition to applying a buoyant force on the particles in proportion to the disparity in density between the microparticle and the medium. Lower-density particles levitate at higher altitudes than higher-density ones.[18] Particle size, shape, chemical makeup, and mechanical characteristics like viscosity, elasticity, and hardness have no bearing on levitation height. Imaging equipment should be used to measure the levitation height of objects once they are suspended. Among the imaging methods frequently employed for this purpose are optical, fluorescent, and inverted microscopy techniques. The next steps are to acquire images and interpret the levitating items. It can take a lot of time to classify, analyze, and quantify the massive volumes of data that are obtained (from high-throughput microscopes). Magnetic Levitation (MagLev) setups can automatically adjust to new trials thanks to machine learning (ML) techniques, which eliminate the need for explicit programming for each use case.[19]

A straightforward yet effective levitational image cytometry tool is described that works for both inverted and upright fluorescence microscopes and provides high-resolution cell population monitoring as well as real-time, label-free separation. A microcapillary tube with identical poles facing each other is positioned between two permanent magnets as part of the experimental setup. Two gold-coated mirrors are positioned at a 45-degree angle for imaging using traditional microscopy. Within a 1 mm capillary, this apparatus was able to separate cells.[20]

Traditional flow cytometry techniques no longer require manual preprocessing and labeling processes thanks to a new technology called CellLEVITAS. In a microfluidic system, live and non-viable cells were separated using the magnetic levitation approach. Under a magnetic field, viable and nonviable breast cancer cells were first separated using levitation conditions. It was then shown that using a range of cell concentrations and input purities, cells could be effectively separated from diverse input purities (10–50%) to constant high-purity output (>80%).[21]

i-LEV, a different smartphone-based MagLev imaging device, provides a magnetic levitation-based diagnostic solution that separates cells according to their distinct densities by levitating them in a magnetic gradient. It has been demonstrated that this technique can count cell numbers and distinguish between white and red blood cells without the need for labels. It is made up of several magnets, mirrors, capillary tubes, and imaging components (the sample is illuminated by LEDs, the smartphone camera lens focuses, and the filters improve the captured photos).[22]

Typically, an intelligent imaging flow cytometer (IIFC) integrates artificial intelligence, imaging technology (such as laser/image sensors), and flow cytometry (Figure 1.3). The system can identify features of a single cell between hundreds and millions of cells every second, while also supporting multi-parameter analysis and high-capacity identification. Additional potential uses for biosensing, including clinical diagnosis make extensive use of IIFC. Accurate cell characterization in cytometry data analysis requires the detection of specific features. Conventional methods for ML and computer vision (CV) have been employed. New algorithms have been created recently to detect and divide rare cells nuclearly.[23] High accuracy automatic cytometry data analysis is provided by these algorithms. These days, software for processing cytometry data uses these conventional ML and CV techniques extensively. Open-source programs like ImageJ and CellProfiler are also utilized. The pipeline works by first loading cytometer-taken images into software, processing them, and then sending them to machine learning systems.[14]

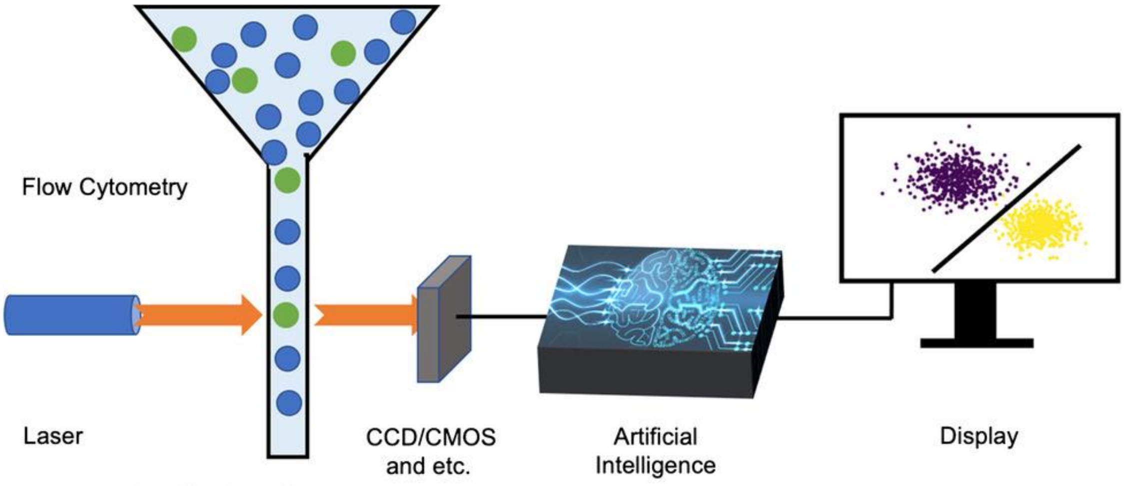

Figure 1.3. Illustration of intelligent image-based cytometry.[24]

Several studies have recently demonstrated how the combination of traditional and deep ML techniques improves the effectiveness of complex systems that provide cell classification. To resolve the issue of locating and sorting the correct cells in real time,[25] developed a method that combines these approaches. Using this method, the main characteristics of bright field images are extracted after binary masks are created, thereby taking advantage of the high accuracy of neural networks. Morphological features and fluorescence intensity data are included, in addition to standard computer vision algorithms for tasks like noise reduction and edge detection. Convolutional neural networks receive the acquired data, which allows for the achievement of high accuracy and speed.[26]

Deep learning algorithms for enhancing microscopy performance have been developed extensively during the previous few years. Deep learning has made it possible to reconstruct three-dimensional images, paint virtually, achieve super-resolution, and achieve single shot autofocus, among other things. Techniques for deep learning-based microscopy enable overcoming optical constraints like the diffraction limit. IFC can benefit from a variety of deep learning applications in cell biology.[27]

Microfluidic systems have several benefits over cell-based analyses, such as smaller instrument footprints, lower sample/reagent consumption, less expensive units, and simpler implementation in remote locations. The advancement of flow cytometers that are microfabricated has drawn a lot of interest recently because they combine inexpensive optical components with the ability to swiftly compute cells and analyze cellular populations at the level of individual cells.[28]

New high-throughput platforms that combine the spatial resolution of optical combining the considerable efficiency of traditional flow cytometry with microscopy methods can be developed thanks to the creation of microfluidic flow cytometers based on images. As mentioned, there are a lot of benefits to integrating an imaging technique with a flow cytometer. Analysis of cellular morphology is crucial for identifying and assessing different disease states.[29]

A microfluidic chip paired with a pair of ring magnets makes up the pump-free microfluidic MagLev platform, which is described in one study as allowing for quick and accurate density determination of individual cells with small sample quantities. Within 16 seconds, the platform permits tiny volumes of liquid (about 4 μL) to naturally distribute in the microchannel. By recognizing levitation profiles and differentiating diverse cell populations, it efficiently characterizes cell densities. It was also utilized to compare A549 lung cancer cells treated with various gefitinib concentrations, providing an automated, portable, and affordable in vitro tool for customized treatment. This method is suggested as a substitute for the upcoming microfluidic device for cell density analysis, manipulation, and characterization.[30]

1.2. Aim of The Thesis

This thesis aims to develop a novel image-based cytometry approach that uses deep learning for analysis to measure the density of microparticles under flow conditions within a microfluidic chip positioned on a magnetic levitation platform. Additionally, to enable the use of this system for sorting purposes, studies were conducted on simple, fast-to-fabricate, and inexpensive microvalves. In this context, Chapter 2 explains the deep learning-based cytometry technique, demonstrating the automatic levitation results for beads of different densities and dead/live human monocytic cells (U937) using the deep learning method. Chapter 3 focuses on the fabrication and optimization of micropneumatic valves, showing leakage tests conducted at different pressures and speeds.

CHAPTER 2

MAGNETIC LEVITATION-BASED CYTOMETRY IN A MICROFLUIDIC CHIP VIA DEEP LEARNING TECHNOLOGY

This chapter presents a unique image-based cytometry method that uses deep learning analysis to quantify the density of microparticles under flow conditions within a microfluidic chip placed on the MagLev platform. Deep learning was described in full in this context. After that, the designed platform and the magnetic levitation principle were described. Following an explanation of the deep learning technique and its performance indicators, the results from the experiments using the bead and cell were discussed.

2.1. State of the Art

2.1.1. Deep Learning Based Cytometry Technologies

The ability of machines and programs to replicate human cognitive experiences and practical patterns is referred to as artificial intelligence (AI).[31] ML a branch of AI, can enhance its analysis using computational algorithms.[32] ML examines learning through behavior, definitions, examples, and narration. Techniques within ML algorithms include categorization analysis, predictive modeling, reinforcement learning, and data clustering.[33,34] DL a branch of ML, imitates the architecture of the brain's neural networks. Computers can learn from hierarchical data representations thanks to DL, which identifies and modifies features using many layers of nonlinear processing units.[35,36] DL has fabricated significant advancements in the field of CV and medical image processing.[37] In CV, DL has addressed issues such as action recognition, motion tracking, object detection, human pose estimation, and semantic segmentation. In medical image processing, The three main categories of DL are segmentation, detection, and classification.[38,39] Convolutional neural network (CNN) stands out as a representative algorithm of DL and is frequently used in the analysis of high-dimensional data covering tasks such as object detection.[40] One of the primary reasons for the preference for CNN is its strong capability to extract local features from images.[41] CNN extracts features directly from a raw series of image data, where the relevant features are not pre-trained. This automatic feature extraction method constitutes the most accurate learning model for visual computing tasks like object detection, classification, and recognition.[42] Contrary to CNN, which converts two-dimensional image data into one-dimensional data during training, resulting in the loss of spatial information, CNNs maintain spatial structure, facilitating the learning of spatial features among pixels. Moreover, CNNs decrease training duration by minimizing the parameter count.[43]

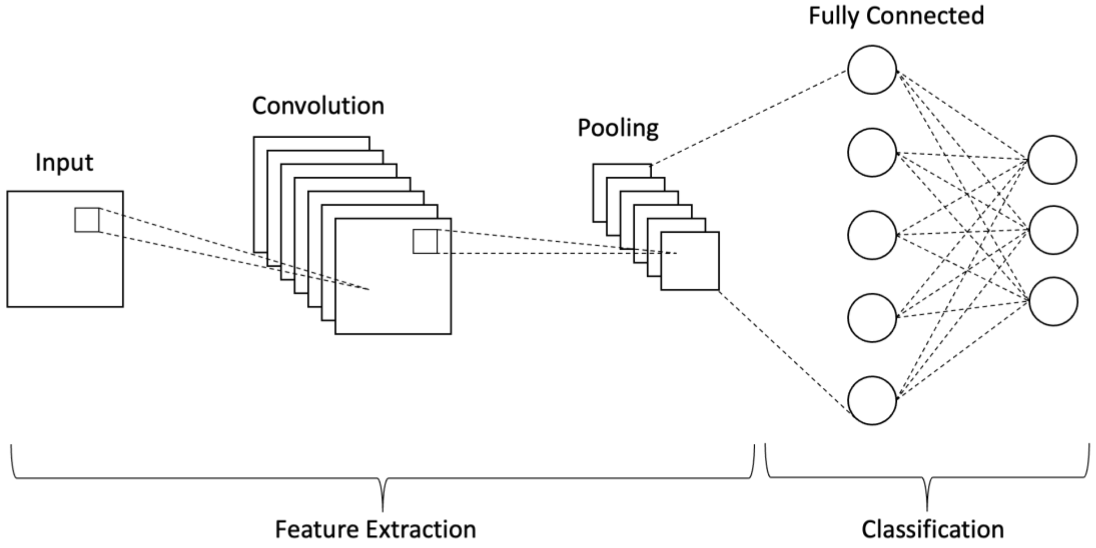

Figure 2.1. CNN Architecture.

CNNs consist of three key layers: convolutional layer, pooling layer, and fully connected layer (Figure 2.1). The convolutional layer creates feature maps by applying a nonlinear activation function after learningable filters to conduct convolution operations across the input volume.[44] Pooling layer cuts down the spatial dimensions of feature maps to reduce computational complexity and capture key features. Common methods are max pooling, which selects the largest element, and average pooling, which considers all elements in the region.[45–47] Fully connected layer functions as the classifier by connecting all neurons from the previous layer, producing the final output of the CNN.[48]

One-stage detectors and two-stage detectors are the two types of deep CNN-based object detection algorithms. Creating candidate boxes and basing predictions on them constitute the two stages of the detection process in two-stage detectors.[49] Although the speed and accuracy of detection have improved with the development of two-stage detectors, many real-time scenarios still cannot be met by them. The development of two-stage detectors has progressively combined separate modules, like feature extraction, bounding box regression, and candidate box generation, into a single end-to-end learning framework in object detection systems.[50] On the other hand, one-stage detectors, including the 2016-proposed You Only Look Once (YOLO), do not require the creation of candidate boxes at the beginning of the process. Rather, they consider location information as indicative of potential objects and proceed to classify each region as either a background or a target object (Figure 2.2).[51] YOLO typically uses the full image to make predictions. In contrast to other methods, YOLO takes the whole image into account both in the training and testing stages. This enables it to implicitly encode contextual information about the images' appearances in addition to their classes.[52] Moreover, YOLO makes object detection predictions in a single stage, which accelerates the YOLO architecture significantly.[53,54] These arguments suggest that YOLO will inevitably be used in cytometry techniques.

DL is applied in various diagnostic techniques, including positron emission tomography, MRI, x-ray, computed tomography, and mammography. Consequently, radiological research has leveraged decades of human expertise, particularly through medical image processing, which aids in identifying and extracting features that are imperceptible to the unaided eye.[55] A novel approach utilizing DL for the detection of red blood cells (RBCs) with nuclei has been proposed due to its remarkable performance in visual recognition. This label-free detection method integrates visual object recognition with Raman spectroscopy on a single cell to rapidly identify nuclear erythrocyte derived cells within complex cell mixtures in real-time.[56]

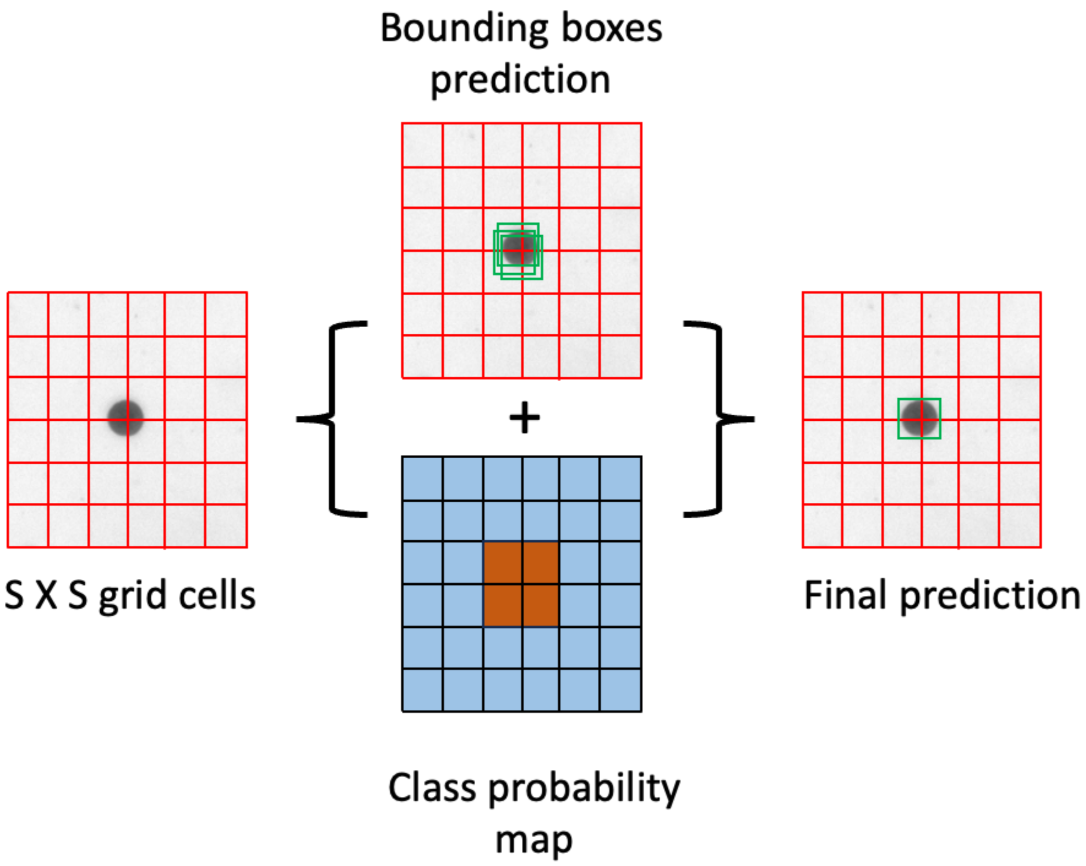

Figure 2.2. YOLO algorithm's working principle. First, an input image is split up into S × S grids. Subsequently, a class probability map (where cells containing objects in the bead class are highlighted in blue) and several bounding boxes are predicted to produce the final bounding boxes and object class.

A platform has been developed for intelligent cell sorting activated by images, integrating DL-based microfluidics in another study. On this platform, cell separation is conducted by utilizing protein localization and image classification.[57] The automatic detection of distinct cell types in microscopy images has achieved heightened success through novel methods employing deep learning architectures. Consequently, a variety of computer-aided cell detection techniques are advocated.[58] These studies underscore the accessibility of deep learning as a tool that aids biologists in comprehending imaging data.

A rapid image processing pipeline system based on deep learning has been developed for label-free IFC on a microfluidic chip using high-throughput microscopy.

By employing just a microscope and a high-speed camera, individual images of cells in flow were captured to perform single-cell analysis in real-time. Particles of various sizes, RBCs, and K562 human leukemic cells were successfully analyzed in the experiments with a dependable accuracy (93.3% mAP). They said that a potent tool for clinical and biomedical applications is anticipated to be the system created following this study.[59]

In one study, flow cytometry waveforms were directly processed using a deep CNN with quick inference. With the deep CNN model, white blood cell and epithelial cancer cell classification was completed in just a few seconds or less. It opened a new avenue for label-free real-time use when it was shown label-free within the microfluidic channel with over 95% accuracy.[60]

2.2. Materials and Methods

2.2.1. Fabrication of the MagLev Platform and Microfluidic Chip

The platform was designed to accommodate two magnets and a microfluidic chip. Arms were added to secure the platform to the microscope stage with M3 screws at the four corners, ensuring it remains stable and upright on an inverted microscope (Figure 2.3 a). The technical drawing was created using AutoCAD (2023) software. The platform was fabricated using a 3D printer (Formlabs Form 3) with Clear resin at a resolution of 0.025 mm. To get rid of any untreated resin, the printed object was submerged in isopropyl alcohol for thirty minutes. The holder was printed to prevent the channel from moving, and the holder was cleaned with the same method (Figure 2.3 b). Neodymium, iron, and boron (NdFeB) magnets of grade N5 5 mm height x 2 mm width x 25 mm length were glued onto the platform facing one another with the same poles in each case. The distance between the magnets glued to the platform was measured as 1.8 mm (Figure 2.4).

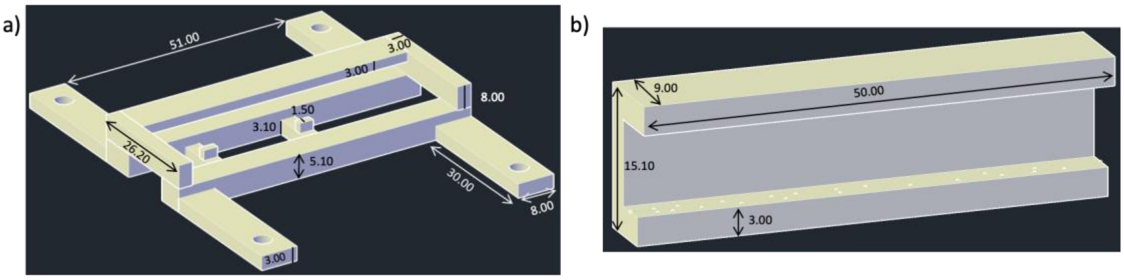

Figure 2.3. 3D images of the molds of (a) platform, and (b) holder. The unit of measurement is in mm.

The fluidic channel consists of an inlet channel and two separate outlet branches at a 45-degree angle. The inlet channel has a width of 1.00 mm, a length of 30 mm, and a height of 0.150 mm. The two output arms have a width of 0.8 mm, a length of 5 mm, and a height of 0.150 mm (Figure 2.5).

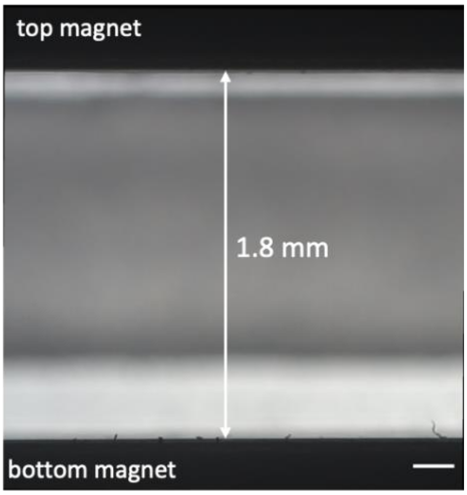

Figure 2.4. Microscope image showing the distance between two magnets. Scale bar: 200 µm.

The mold has the same width and height as the cover glass (0.17 mm height × 24 mm width × 60 mm length) to ensure that the polydimethylsiloxane (PDMS) channel removed from the mold adheres to the cover glass. The technical drawing of the mold was created using AutoCAD (2023) software. A 3D printer (Formlabs Form 3) was used to print the mold (Figure 2.6) using High-Temperature V2 resin at a resolution of 0.025 mm. They were washed in isopropyl alcohol for 10 minutes, followed by a post-cure process at 80ºC for 120 minutes.

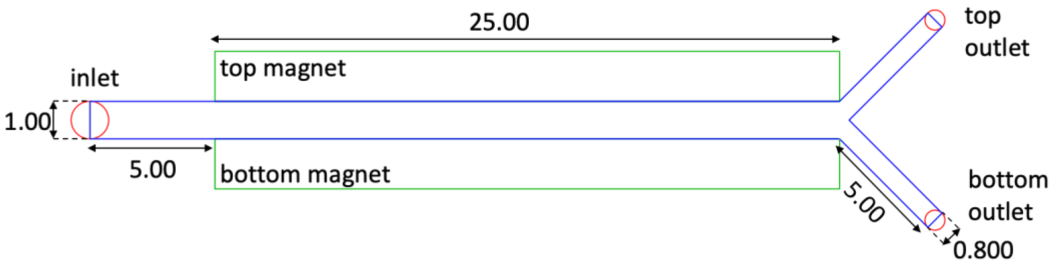

Figure 2.5. The drawing of fluidic channel. The units of measurement are in mm.

To eliminate air bubbles, PDMS was made with an elastomer/curing agent ratio of 10:1, and it was vacuum sealed for two hours. The PDMS-cast mold was then cured at 100°C for 1 hour. Subsequently, the fluid channel was removed from the mold using tweezers, and the inlets were punctured with a 15-gauge needle (inner diameter = 1.372 mm, outer diameter = 1.829 mm). To bond the cover glass and fluid channels, air plasma (ZEPTO, Diener) was applied to the relevant surfaces at 100 W and 0.5 Torr for 1 minute. As a result, a microfluidic chip was obtained (Figure 2.7).

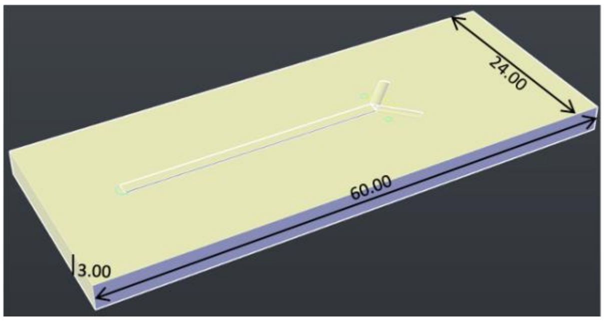

Figure 2.6. 3D image of the mold of the fluidic channel. The unit of measurement is in mm.

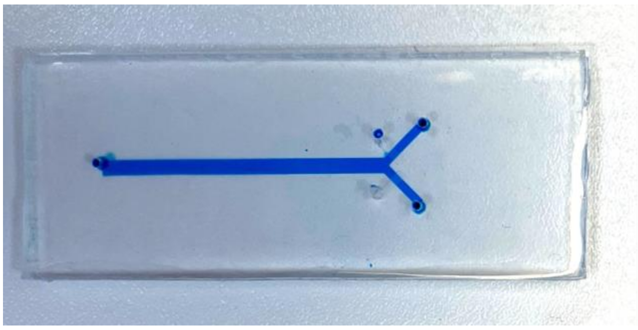

Figure 2.7. The photograph of the microfluidic chip. The microfluidic channel was filled with blue colored food dye solution.

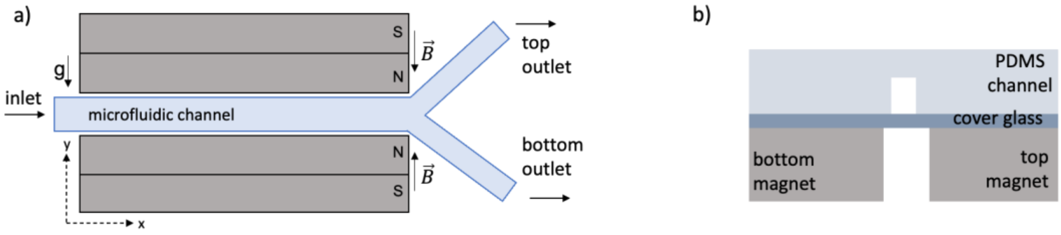

Figure 2.8. Magnetic levitation-based platform. (a) Top and (b) cross-sectional views of the microfluidic chip placed on the two opposing magnets.

The microfluidic chip was placed on the platform, directly above the magnets, and the fluidic channel was in the middle of the two magnets and fixed with a holder (Figure 2.8). It was then placed on the inverted microscope with the help of screws (Figure 2.9).

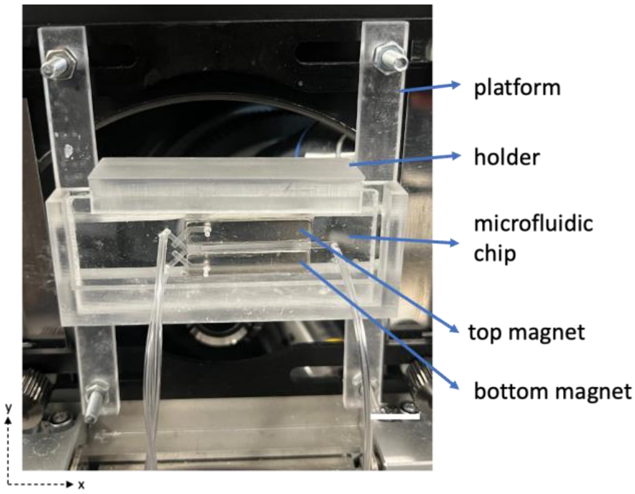

Figure 2.9. A photograph of the platform on an inverted microscope.

2.2.2. Magnetic Levitation Principle

Samples of cells or beads were made to levitate inside the microfluidic channel on the magnetic levitation platform by using an ionic paramagnetic solution (Gadavist) sandwiched between two opposing magnets.[61,62] With this technique, differing densities of cells or beads can be separated without the requirement for labeling.[63] The weakest magnetic field, situated midway between two magnets, attracts cells or beads on a magnetic levitation platform. The cells become motionless at this moment when the buoyancy and magnetic forces are equal,[64] as the following equation illustrates:

$$F_{mag} = \frac{V(\chi_c - \chi_m)}{\mu_0} (B.\nabla)B + V(\rho_c - \rho_m)g = 0 \quad (2,1)$$

Here, χ_m andχ_c represent the magnetic susceptibilities of the paramagnetic medium and cells, respectively. μ_0 is the permittivity of free space (vacuum) and its value is 1.2566×10^{-6} kg·m·A^{-2} ·s^{-2}. B denotes magnetic induction (T). ρ_m and$\rho_c$are the densities of the medium and cells or beads, and g represents the gravitational acceleration (9.8 m·s^{-2}). V represents the cell's volume. Furthermore, in comparison to the paramagnetic solution, the cells' magnetic susceptibility (χ_c) is minimal.

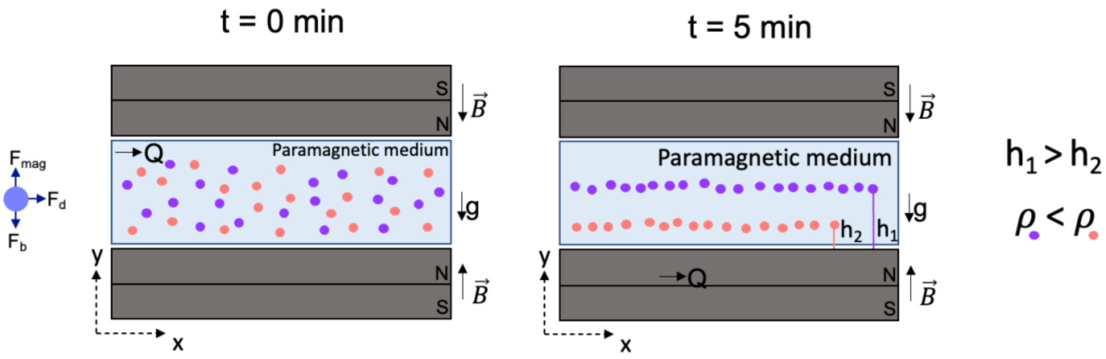

Figure 2.10. Principles of magnetic levitation. Under magnetic (F_{mag}) and buoyant (F_b) pressures, beads were levitated to a stable height (h_1, h1) dependent on their densities (ρ), then they were dragged (F_d) under a flow (Q). B and g represent the magnetic induction and the gravitational acceleration, respectively.

Stated differently, the density of the cells is what causes them to exhibit different levitation heights within the same environment. Denser cells on the platform hover toward the bottom magnet. The bottom magnet is used as a reference, and the distance between the bottom magnet and the cell is measured to establish the levitation height of the cell (Figure 2.10).[65,66]

2.2.3. Objet Detection Performace Metrices

As shown in Figure 2.11, the intersection is the area where the anticipated bounding box and the overlap with ground truth, and the union is the total area between the two.[67] The intersection of the actual and predicted bounding boxes of objects in the dataset is measured by the Intersection over Union (IoU) technique. The area of intersection between the predicted and ground truth bounding boxes, as well as the total area of both boxes, are divided to determine the IoU. It accepts values in the range of 0 to 1, where a value nearer 1 denotes a more precise object detection. It's a measurement method for locating errors in object detection models' localization.[68]

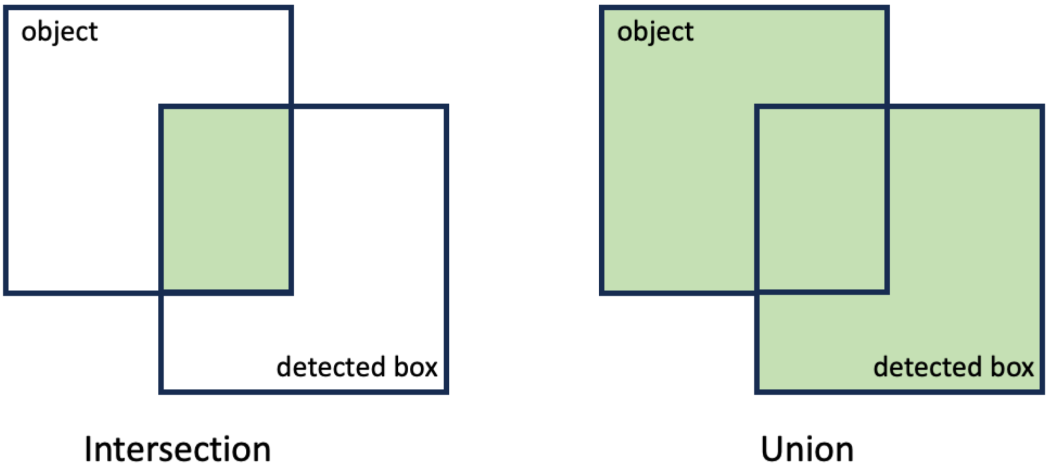

Figure 2.11. Definitions of intersection and union are illustrated.

In this study, the number of beads that were correctly identified as beads was represented by True Positive (TP), which was a measure of the dataset used to detect beads. The quantity of beads that were misidentified as beads was known as False Negatives (FN), False Positives (FP) on the other hand were the number of non-bead cases that were incorrectly identified as beads.[69]

Precision is the accuracy of the model's positive predictions. Equation 2.2 displays the formula used to calculate the precision. The percentage of actual good examples that the model properly detected is known as recall, and Equation 2.3 provides the procedure for doing so. The accuracy of the model in detecting objects at various degrees of precision is gauged by the commonly used parameter known as average precision (AP). For various thresholds, it computes the region beneath the accuracy-recall curve.[70,71] The mean AP score over several classes is provided by mAP. In general, mAP is regarded as a crucial performance indicator for object detection. The mAP at an intersection above the IoU threshold of 0.5 is specifically measured by mAP@0.5.[72]

$$Precision = \frac{TP}{TP + FP} \tag{2.2}$$

$$Recall = \frac{TP}{TP + FN} \tag{2.3}$$

Equation 2.4 defines the F_1 score, which was chosen as an equilibrium between recall and precision to better illustrate the model's overall performance. A value ranging from 0 to 1 represents the F1 score, where 1 represents the best possible performance.[73]

$$F_1 = \frac{2 \times Recall \times Precision}{Recall + Precision} \tag{2.4}$$

2.2.4. Calculation of Levitation Height with YOLO

The bounding boxes of the anticipated beads from the YOLO model were used to compute the levitation height and radius of the beads. The bounding box provides the width, height, and coordinate values of the upper-left corner. The height and the y-coordinate value were used to determine the middle of the bounding box. Additionally, the coordinate values for the bottom magnet's upper border were established. The levitation height was found by calculating the difference between the two. Additionally, half of the height of the bounding box was taken as the bead radius (Figure 2.12).

The object detection was performed using Python (3.10) in PyCharm software (2022.2.4) with the OpenCV, ultralytics, matplotlib, and collections libraries. The below Python code tracks particles in a video file using the YOLOv8 model, calculates their levitation heights and particle radii, stores them, and visualizes the results. The code that automatically calculates the levitation height is given in Appendix A.

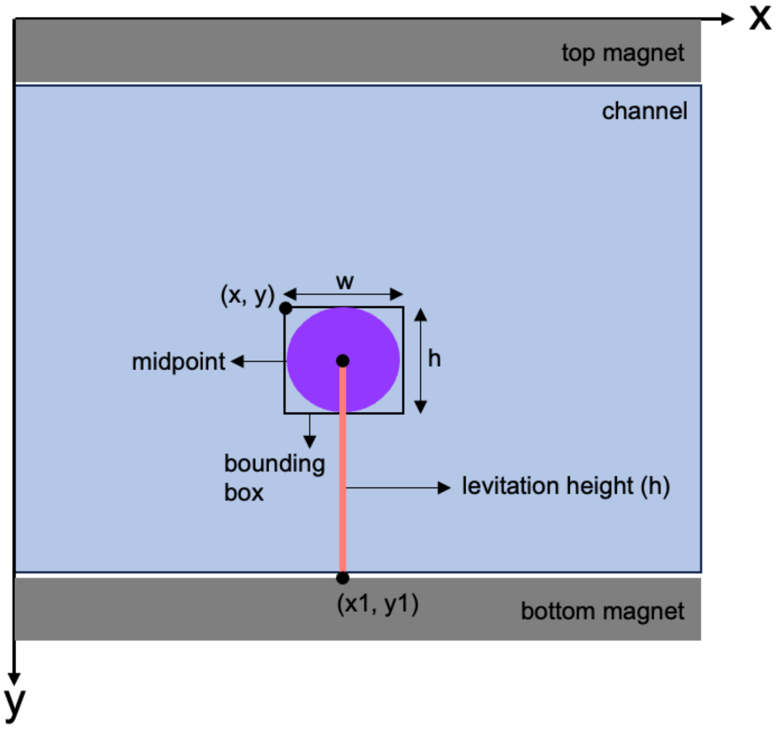

Figure 2.12. YOLO was used to determine the bounding box of the detected bead. The levitation height (i.e., the distance between the bottom magnet and the bounding box midpoint) and radius (i.e., half of h) of the bead were determined using the bounding box's width (w), height (h), and upper left corner (x, y) coordinates.

Initially, necessary libraries are imported, and a pre-trained model (`best.pt`) along with a video capture object from the video file path is loaded. A video writer object is set up with specified parameters, and a `defaultdict` named `track_history` is created to store tracking history. The magnet location is determined, and video frames are processed in a loop. In each frame, the YOLOv8 model performs tracking, and the detected boxes and tracking IDs are obtained. The levitation height and radii of the particles are calculated and added to the `track_history` dictionary. The marked frame is saved to the video writer and shown on the screen. The loop terminates when either the video concludes, or the q key is pressed. Tracking data, including average levitation heights and particle radii, is written to a text file and graphs are plotted and saved. Finally, resources are released, and all open windows are closed.

In the code, images were collected on a platform mounted on an inverted microscope (Olympus CKX53) with a 4x lens and a camera (FLIR Blackfly S) to obtain the "best.pt" file. 40 microfluidic channel images containing beads of different densities (1.09 g/mL, 1.05 g/mL, and 1.02 g/mL) were used, with 70% for training, 20% for validation, and 10% for testing. The beads in the micrographs were annotated with bounding boxes in the form of bead classes using Roboflow (Roboflow Inc., USA). The file from Roboflow was then trained using a Google Colab Notebook (interactive code editor). The training parameters were selected as a batch size of 16 and 250 epochs, respectively. YOLOv8 models were chosen to achieve the best training result and the highest mAP@0.5. The parameters and methods used for bead training were also applied to cell training. A total of 175 microscope images of MDA-MB-231 cells were annotated using Roboflow, with 70% for training, 20% for validation, and 10% for testing.

In the code that automatically calculates the levitation height, the coordinate information of the upper limit of the lower magnet is needed. For this purpose, the magnet-focused microscope image was obtained with a code that gives the position of the point where the computer mouse was clicked. This code uses OpenCV to allow users to draw and manage circles on an image through mouse clicks. First, an image is loaded from the specified file path, and if loading fails, the program terminates. An image copy of the original is made for the drawing operations. A window is created to capture mouse clicks, and the `mouse_drawing` function is assigned to handle these events. This function draws red circles at the clicked coordinates and adds these coordinates to the `circle's` list when the mouse's left button is depressed. The `draw_circles_on_image` function draws circles based on the coordinates in the `circles` list and displays the updated image. An infinite loop waits for keyboard input; pressing the `q` key terminates the program while pressing the `w` key clears all drawn circles and resets the screen. This setup provides a basic application for image processing and user interaction. The code is given in Appendix B.

2.2.5. Sample Preparation

Polystyrene beads of various densities (1.00 g/mL for 10-20 μm size, 1.02 g/mL for 10-20 μm size, 1.05 g/mL for 45-53 μm size, and 1.09 g/mL for 20-27 μm size, from Cospheric, LLC) were suspended in phosphate-buffered saline (PBS, Gibco) with 0.1% (w/v) Pluronic. A 20 μL solution containing 50 mM Gd^{3+}, a paramagnetic substance, was then pipetted into the channel. Beads with densities of 1.02 g/mL and 1.09 g/mL were also introduced into the channel using 20 μL pipette solutions containing Gd^{3+} concentrations of 25, 50, and 75 mM.

U937 human monocytic cells were cultured in RPMI-1640 medium (Euroclone) supplemented with 1% Penicillin-Streptomycin (Euroclone) and 10% fetal bovine serum (ECS0180, Euroclone) at 37°C with 5% CO_2. Mature U937 cells were centrifuged at 1000 rpm for 5 minutes, the resulting cell pellet was resuspended in fresh medium, and adjusted to a quantity of 10^5 cells per milliliter.

U937 cells were prepared by centrifuging at 1000 rpm for 5 minutes, then resuspended to a density of 105 cells per mL in RPMI medium. Dead U937 cells were obtained by adding 1:1 (v/v) dimethyl sulfoxide (DMSO, Sigma Aldrich) to the cell medium, followed by a 15-minute incubation. Prior to experiments, the cell medium was replaced with PBS containing 0.1% (w/v) Pluronic. MagLev experiments were conducted on both live and dead cells by adding Gd^{3+} at concentrations of 100 mM, 150 mM, and 200 mM.

MDA-MB-231 human breast cancer cells were cultured in Dulbecco's Modified Eagle's Medium (DMEM, Gibco) supplied at 37°C with 5% CO_2 in addition to 10% FBS and 1% Penicillin-Streptomycin. Upon achieving sufficient growth, the culture supernatant was removed, and cells were detached using Trypsin-EDTA (Euroclone) and incubated at 37°C for 10 minutes. Detached cells were centrifuged at 1000 rpm for 5 minutes, and the resulting cell pellet was transferred to a new flask with a fresh medium.

To ready MDA-MB-231 cells for the experiment, they were centrifuged at 1000 rpm for 5 minutes. Next, the resultant cell pellet was adjusted to a concentration of 10^3 cells per mL in RPMI culture medium. MagLev experiments were conducted on these cells by introducing Gd^{3+} at concentrations of 50 mM, and YOLO training was carried out using the captured images.

2.2.6. Statistical Analysis

All experiments were conducted a minimum of three times. Results are expressed as mean ± standard deviation (SD). The coefficient of variation (CV%) was calculated as the standard deviation divided by the mean, representing variability across and between experiments. Statistical significance was assessed using two-way analysis of variance (ANOVA) with Sidak post hoc correction, conducted using GraphPad Prism version 9.2.0 (GraphPad Software). The OriginLab workspace's 2D Confidence Ellipse application was utilized for confidence ellipses. For every treatment, scatter plots were enabled, and each scatter plot had a 95% confidence level specified.

2.3. Results

2.3.1. Magnetic Levitation of Beads and Cells

To calculate the heights of the beads, images were taken every 5 minutes for the first 15 minutes and then every 15 minutes thereafter. Statistical analysis of the 15-minute intervals did not show a significant difference, similarly, no significant difference was observed with the 5-minute intervals (Figure 2.13). Additionally, it was demonstrated that beads of different densities exhibited different levitation heights (Figure 2.14). In subsequent experiments, 1.02 and 1.09 g/mL densities of beads were used for analysis with YOLO. Microscope images at 0 and 5 minutes in 50 mM Gd^{3+}, demonstrating their equilibrium, are shown in Figure 2.15. Considering the channel and magnet lengths, a flow rate of 0.05 mL/h was optimally selected to allow the beads to reach constant lift heights, and then the determined flow was delivered through the inlet via a syringe pump (NewEra Pump Systems, NE-1000).

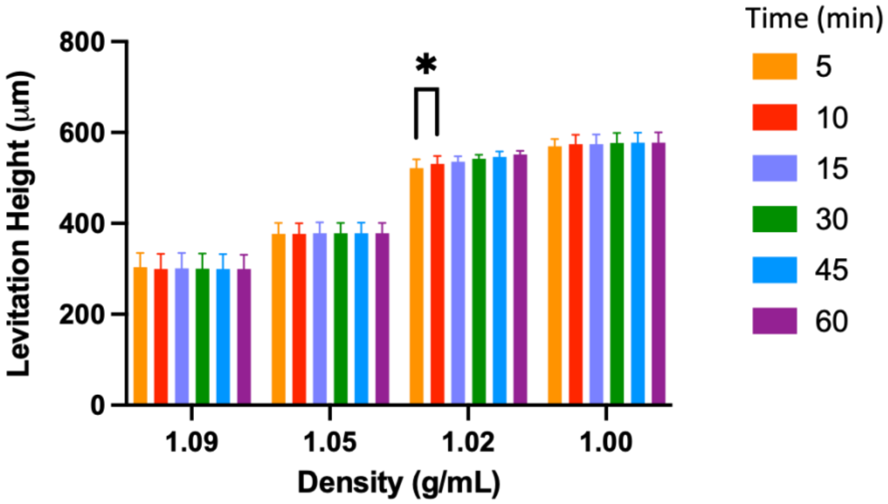

Figure 2.13. Levitation heights of different beads at 50 mM Gd^{3+} concentration at different time intervals. Analysis results were shown at 5-minute intervals for the first 15 minutes and then at 15-minute intervals Comparison results of others do not show any significant difference.

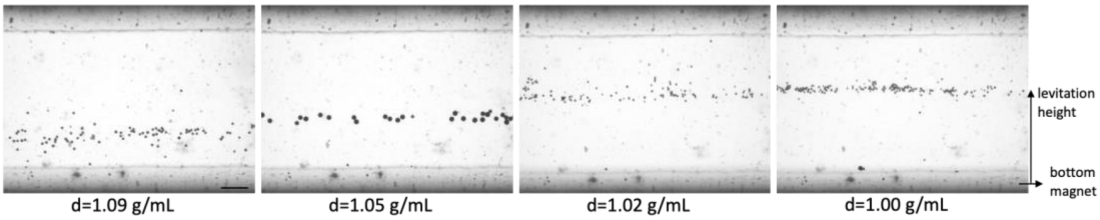

Figure 2.14. Levitation heights of beads with density of 1.09 g/mL, 1.05 g/mL, 1.02 g/mL, and 1.00 g/mL at 50 mM Gd^{3+} concentration in the 5th minute. Scale bar: 100 μm.

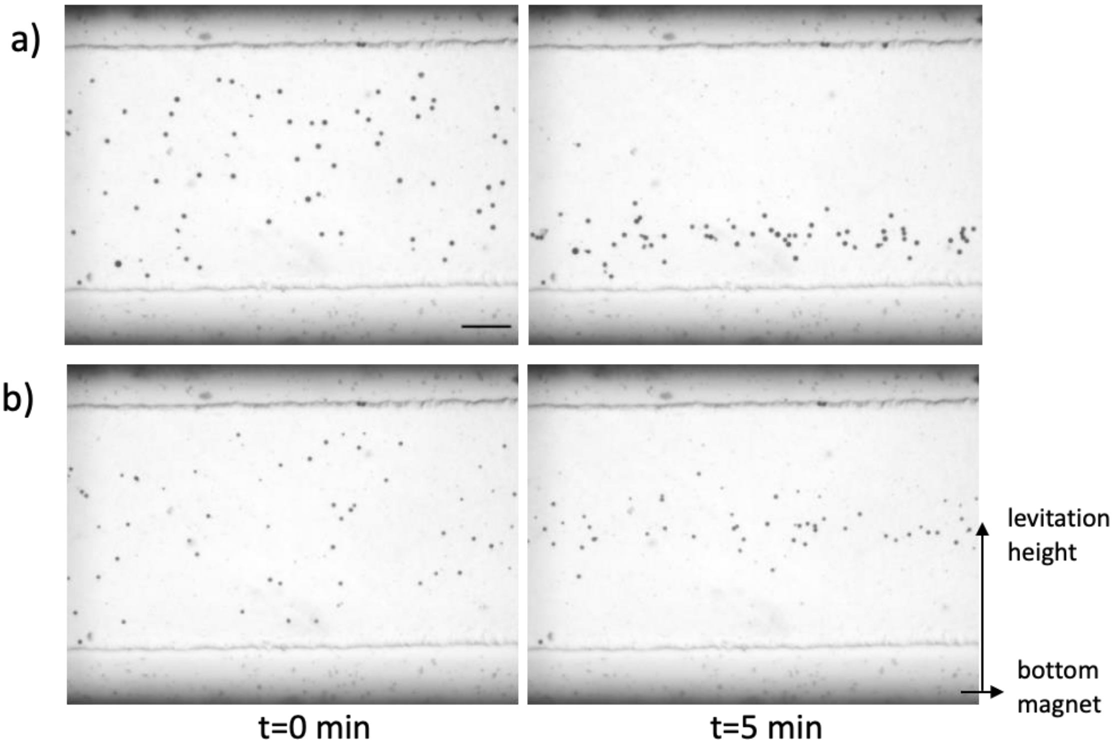

Figure 2.15. Levitation heights of beads with density of (a) 1.09 g/mL, and (b) 1.02 g/mL at 50 mM Gd^{3+} concentration in the 5th minute. Scale bar: 100 μm.

2.3.2. Deep Learning Based Analysis of Beads

TP, FP, TN, and FN were all broken down in detail in the confusion matrix (Figure 2.16). mAP value was found to be 0.99 in the selected YOLOv8s model. Precision and recall values were shown as 0.973 and 0.957, respectively. High precision and recall values showed that the model was well-balanced and worked well at accurately detecting objects while reducing FP and FN. In addition to this, the F_1 score is 0.964, which means that the model was highly efficient in detecting objects with a good balance of precision and recall.

When tested on the microscope image, all 25 beads were successfully detected, and the dust particles were not recognized by the model (Figure 2.17). It showed that performance metrics were consistent with real-time results.

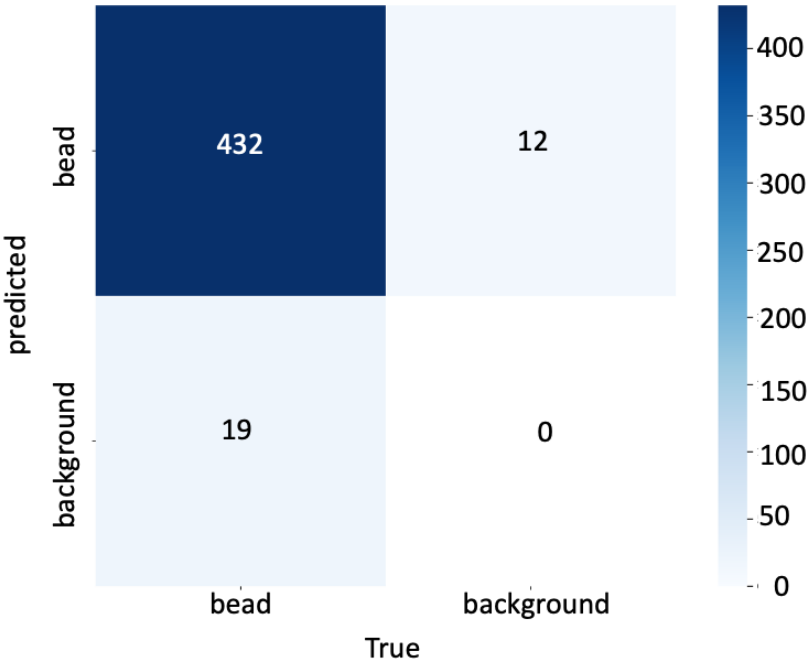

Figure 2.16. Model confusion matrix for both true and predicted classes after training.

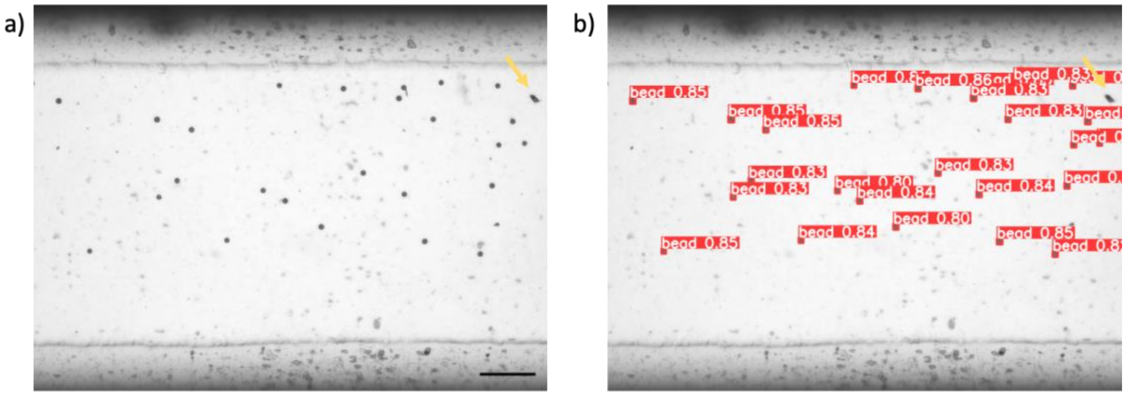

Figure 2.17. Detection of beads. (a) A Micrograph of a microfluidic channel containing 25 beads. Scale bar: 100 µm. (b) Detection of beads shown in (a) with YOLO. Dust particle indicated by an arrow was not detected with YOLO.

2.3.3. Performance of Deep Learning Based Analysis

It was observed that the flow rate is a very important criterion during the detection phase. Bead detection was assessed at flow rates of 0.05 mL/h, 0.1 mL/h, 0.5 mL/h, and 1 mL/h to determine the limits of detectable flow rates. At flow rates of 0.05 mL/h and 0.1 mL/h, all beads were successfully detected (Figure 2.18 and 2.19). However, at a flow rate of 0.5 mL/h, 23.24% of the beads were detected throughout the flow, 27.68% were undetected, and the detection status of the remaining 49.10% fluctuated (Figure 2.20 and 2.21). At a flow rate of 1 mL/h, almost no beads were captured in the frame. While performing bead detection in Python on the video recording, the video was slowed down for processing, and the output was subsequently recorded for a longer duration. The importance of the computer processor was also noted in this process.

at t = 0 s   at t = 8 s   at t = 16 s

Figure 2.18. A video segment of bead detection with a density of 1.09 g/mL using YOLO at a flow rate of 0.05 mL/h.

at t = 0 s   at t = 5 s   at t = 10 s

Figure 2.19. A video segment of bead detection with a density of 1.09 g/mL using YOLO at a flow rate of 0.1 mL/h.

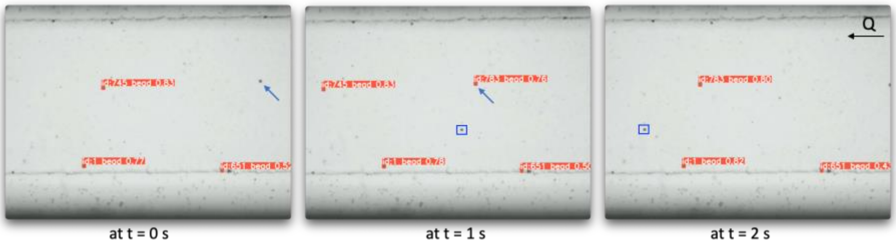

Figure 2.20. A video segment of bead detection with a density of 1.09 g/mL using YOLO at a flow rate of 0.5 mL/h. The bead enclosed in the blue box is not detected throughout the flow, while the bead indicated by the blue arrow is detected after a certain period.

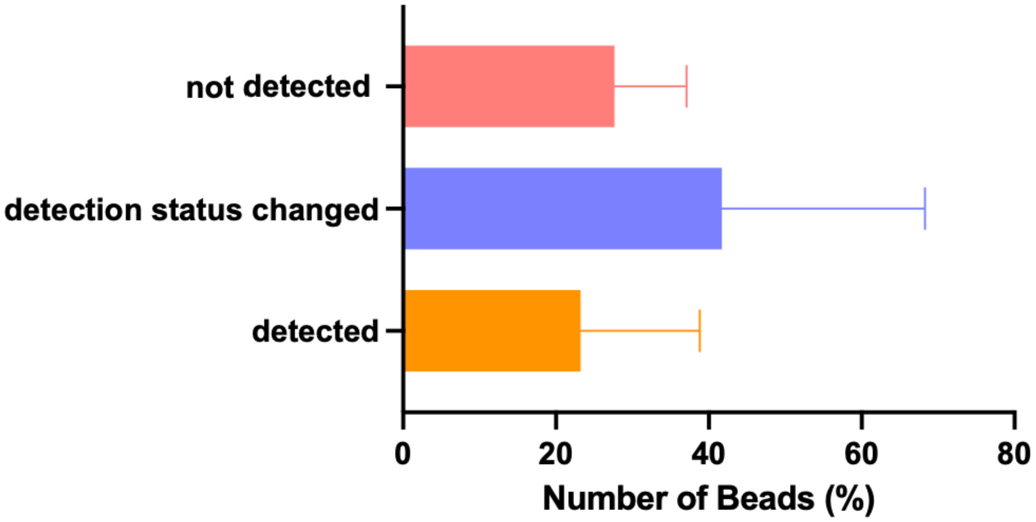

Figure 2.21. The graph of the detection status of beads under 0.5 mL/h flow. It is the percentage representation of the number of beads with densities of 1.09 and 1.02 that are detected under 0.5 mL/h flow, are not detected, and the detection status is constantly changing.

The accuracy of the calculated levitation height and radius values was evaluated at the selected flow rate of 0.05 mL/hour, which was considered optimal for the levitation height. For this purpose, the levitation height and radius of 174 beads were calculated manually using ImageJ software. The obtained values were compared with the levitation height and radius values of beads calculated from the bounding boxes of YOLO. As a result, the coefficient of determination (R^2) between manual calculations for levitation height and YOLO results was found to be 0.9987 (Figure 2.22 a), indicating a very high correlation between the results. It shows that levitation height calculation has been successfully implemented with YOLO. The coefficient of determination (R^2) between manual calculations of bead radius and YOLO results was calculated as 0.9066 (Figure 2.22 b). As a result, a strong correlation was observed. However, small differences at the micron level (0.1-0.7 µm) caused a slight decrease in the R^2 value.

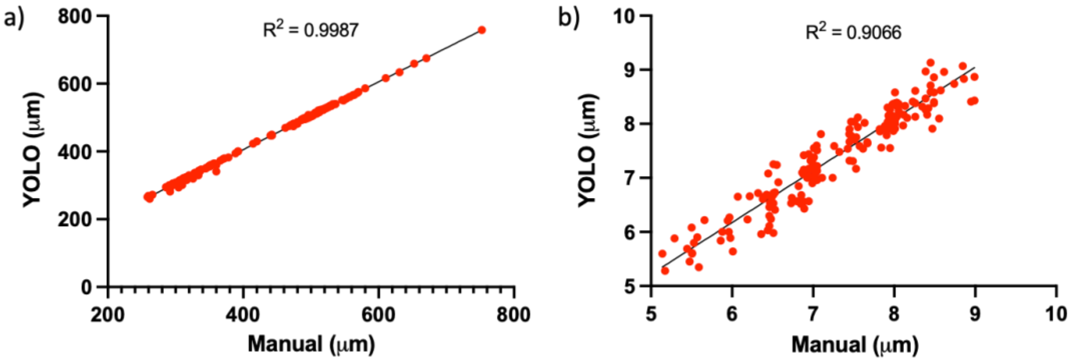

Figure 2.22. Comparison of bead data analysis performed manually and automatically using YOLO. The comparison graphs of (a) the levitation heights and (b) the radius of beads. The figures displayed the coefficient of determination (R^2) values obtained from the linear regression model.

The analysis of beads with densities of 1.02 g/mL and 1.09 g/mL using YOLO showed that both were collected at different levitation heights (Figure 2.23). Also, the beads adhered to the channel wall or surface at the experiments. It prevented the accurate calculation of the levitation height for some beads. These beads were easily distinguishable on the graph as they were outside the main aggregation areas. Aside from these instances, there were no problems in calculating the levitation height accurately.

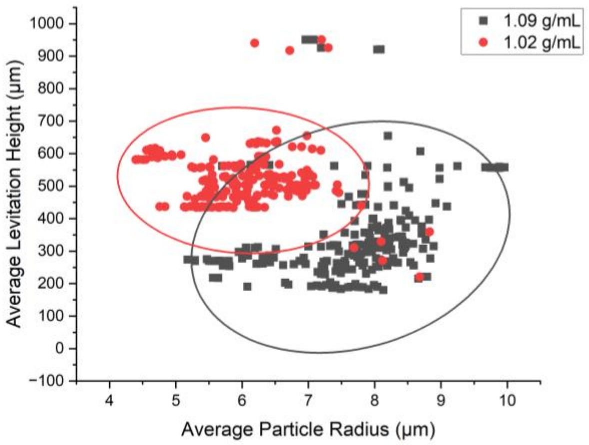

Figure 2.23. Automated analysis of beads with densities of 1.09 and 1.02 g/mL under a flow rate of 0.05 mL/h at 50 mM Gd^{3+} concentration. The 95% confidence ellipse shown in the graph indicates that 95% of the data points will fall within this ellipse.

2.3.4. Deep Learning Based Analysis of Cells

TP, FP, TN, and FN were all detailed in the confusion matrix for detecting MDA-MB-231 (Figure 2.24). In the selected YOLOv8s model, the mAP value was found to be 0.958. Precision and recall values were reported as 0.860 and 0.947, respectively. The precision value indicates that the model exhibits significant reliability in its positive predictions, while the recall value shows that the model correctly identifies most of the TP examples. Additionally, the F_1 score is 0.90, indicating that the model generally demonstrates reliable and effective performance.

When tested with a microscope image of U937 cells, 8 out of 10 cells were successfully detected (Figure 2.25). In the whole image, 58 of 85 cells were detected. The reason for the undetected cells may be that the inside of the cells is transparent and not filled like beads. By enriching the dataset, the model's precision and recall values can be increased.

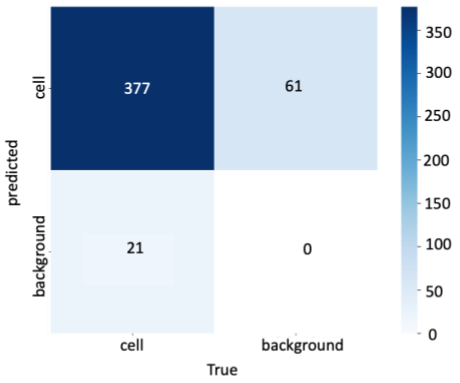

Figure 2.24. Model confusion matrix for both true and predicted classes after training.

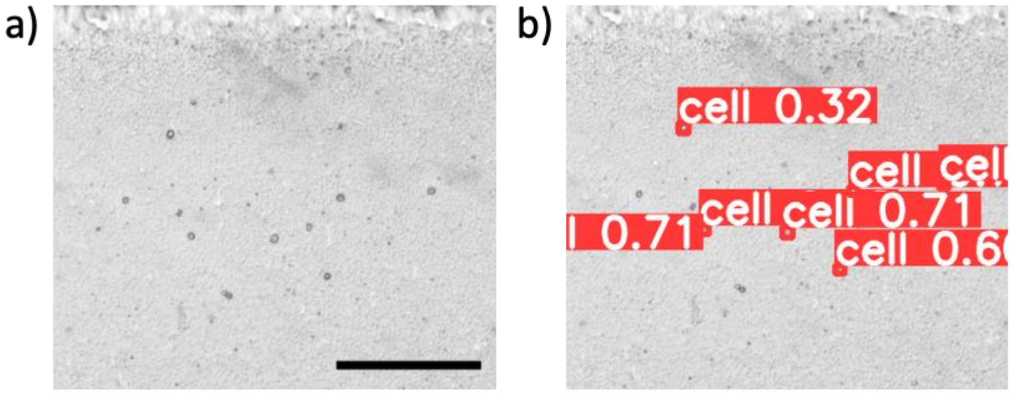

Figure 2.25.Detection of U937 cells. (a) A Micrograph of a microfluidic channel containing cells. Scale bar: 100 µm. (b) Detection of cells shown in (a) with YOLO.

Dead and live U937 cells were sorted at different levitation heights in 100 mM Gd^{3+} (Figure 2.26). When the radius and levitation height analysis was performed using YOLO, the graph showed that dead and live cells clustered at different levitation heights. In addition, dead and live cells are indicated in the graph using GMM clustering, from dark to light, depending on the density of the region in which they are located (Figure 2.27). As a result, dead and live U937 cells could be successfully detected in a label-free manner.

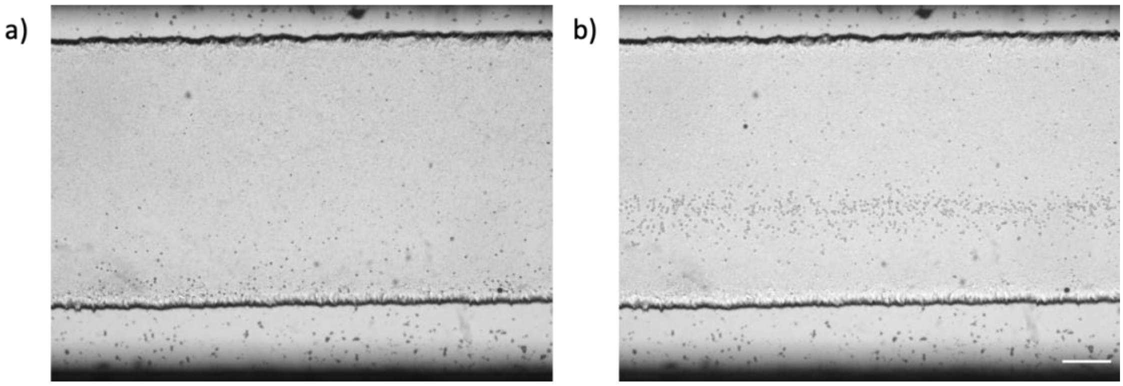

Figure 2.26. Microscopic images of U937 cells at a concentration of 100 mM Gd^{3+} after 5 minutes, showing a) dead and b) live states. Scale Bar: 100 µm.

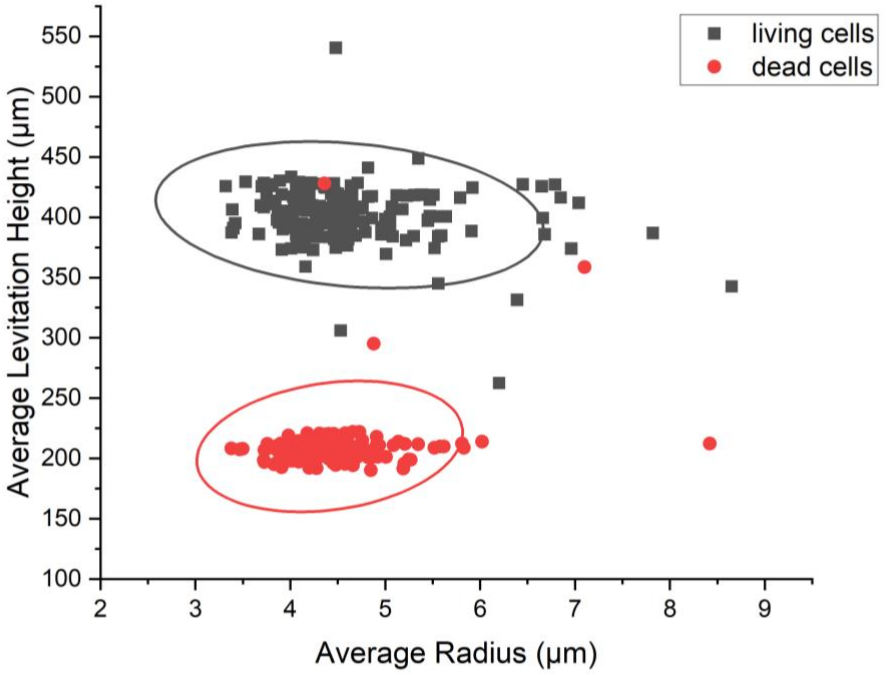

Figure 2.27. Automated analysis of dead and live U937 cells under a flow rate of 0.05 mL/h at 100 mM Gd^{3+} concentration. The 95% confidence ellipse shown in the graph indicates that 95% of the data points will fall within this ellipse.

2.4. Conclusion

As a result, the magnetic levitation platform and microfluidic chip were successfully fabricated. MagLev experiments were conducted with micro-particles of different densities (1.09 g/mL, 1.05 g/mL, 1.02 g/mL, and 1.00 g/mL). It was observed that a duration of 5 minutes was sufficient for the beads to reach equilibrium. Consequently, considering this duration and the dimensions of the microfluidic chip, the flow rate was determined to be 0.05 mL/h. The microscopic images obtained during the experiments were used as a dataset, and training was performed using the YOLOv8s model. The results showed that the precision and recall levels were 0.973 and 0.957, respectively, demonstrating the success of the model. Subsequently, Python code was written for the automatic analysis of the levitation height and radius of the detected beads. When the manual and YOLO results were compared, the determination coefficients (R^2) for levitation height and radius were found to be 0.9987 and 0.9066, respectively. A high correlation was demonstrated between the manual and automatic analyses, indicating that levitation height and radius were successfully calculated. The performance of the automatic detection and analysis method was tested. Beads were successfully detected at flow rates of 0.05 and 0.1 mL/h. On the other hand, at a flow rate of 0.5 mL/h, some beads were not detected at all, and the detection of some varied continuously. At a flow rate of 1 mL/h, no beads were detected. In this context, it was realized that flow rate is an important criterion. Subsequently, MagLev experiments were conducted with beads of densities 1.09 g/mL and 1.02 g/mL. The analysis performed with YOLO revealed that the beads accumulated in two distinct regions, and appropriate cytometry data was obtained. After all necessary optimizations for the micro-particles, cell experiments were conducted. The YOLOv8s model was trained with MDA-MB-231 cells. The model's performance was evaluated, yielding sensitivity and recall values of 0.860 and 0.947, respectively. Subsequently, live-dead MagLev experiments were conducted using the U937 cell line. In the analysis results with YOLO, live and dead cells clustered in different regions. In conclusion, the deep learning method enabled successful bead and radius calculations in a magnetic levitation platform under flow without labels. This approach offers the potential for real-time, label-free, easy, and simple detection of micro-particles and cells in the future.

CHAPTER 3

3D PRINTING-ASSISTED FABRICATION OF MICROFLUIDIC PNEUMATIC VALVES

This chapter describes microfluidics and microvalves. The working mechanism of the pneumatic valve is explained. Various optimization tests have been demonstrated for the design of a pneumatic valve with appropriate dimensions. Afterward, leakage tests were performed on the complex chip design under different flow rates and pressures.

3.1. State of the Art

Microfluidics makes use of structures at the micron scale to precisely control and manipulate small volumes of fluids.[74] The use of minimal sample and reagent volumes, the ability to perform multiple reactions simultaneously for high-throughput analysis, the potential for cost reduction, and the combination of various procedures on a single chip for miniaturization and automation are just a few of the significant advantages that microfluidics offers over traditional analysis techniques. Many microfluidic platforms have been developed as a result of these characteristics for use in clinical and academic settings.[75,76]

Since silicone and glass were first introduced, the main material for creating microfluidic chips has been silicone-based elastomers, specifically PDMS. The ideal material for creating integrated valves is PDMS because of its high gas permeability. Its important importance in cell-related microfluidics has been demonstrated by numerous landmark experiments. Due to its flexibility, and superior optical, and mechanical properties, PDMS remains the most used material.[77]

As technology significantly reduces the time required to transition from concept to chip, a growing number of microfluidic chip manufacturers are using 3D printing. Instead of traditional manufacturing methods such as SU-8 molding in recent years.[78] The ability to easily perform adjustments related to production, testing, and design, and to quickly iterate within a single day through 3D printing, can significantly reduce key operational costs in a clean room environment.[79] Stereolithography, one of the 3D printing methods, allows the production of molds that can produce a wide variety of extremely complex 3D structures with great precision and at affordable costs. A concentrated LED or laser light source is utilized in the well-established process of stereolithography (SL) to create three-dimensional polymer structures from liquid photopolymer resin (Figure 3.1). In SL, photopolymerization occurs layer by layer to create the desired object.[80]

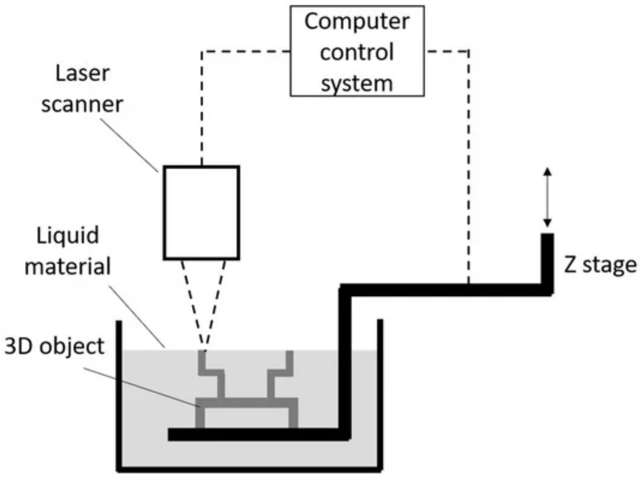

Figure 3.1. Illustration of SL.[81]

One essential component of lab-on-a-chip systems is the manipulation of microfluidics, and numerous techniques have been developed for liquid manipulation.[82] Flow-directing microvalves are among the most important parts of microfluidic devices.[83] Large microfluidic systems with many microvalves have been created for high efficiency and broad functionality because of their robust functioning and ease of fabrication. For applications including microflows, cell analysis, drug development, and physical/chemical detection, microvalves' performance is essential.[84,85] Pneumatic forces, whose applicability for liquid control and actuation has been proven in other microfluidic platforms in the past, have provided a solution for manipulating liquids using air.[86] The use of pneumatic microvalves allows for the instant regulation of flow within microchannels.[87–89] The cross-channel architecture made of PDMS, developed by the Quake group, is a type of micropneumatic valve.[90] This type of valve provides a fast response time and ease of manufacturing. Sample loading and transportation channels are found in the "fluidic layer". Pneumatically actuated valves are formed and controlled via channels that make up the "control layer." There is a small membrane separating these two layers. When the fluidic and control channels intersect with appropriate dimensions and configurations, a valve is formed. By exerting pressure on the upper channel of this design, a thin PDMS membrane is deflected downward, closing the elliptic fluidic channel and halting the liquid flow. (Figure 3.2).[91]

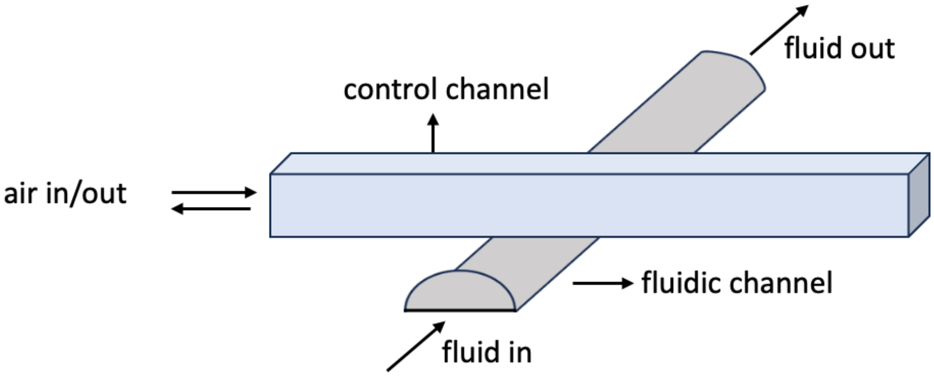

Figure 3.2. Illustration of valve formation with fluidic and control channels.

In a recent study, a method was reported for the creation of an array with just one cell by integrating pneumatic valves with single cell capture zones in a single microfluidic device. These single cells capture zones contain micro barriers in the fluidic channels to trap different cells, allowing for precise control over cell interactions. These findings also demonstrate promise and utility for conducting drug testing efficiently at the level of individual cells. Furthermore, it has been suggested that this approach could act as a potent instrument for various single-cell-based analyses, such as multipurpose immune sensors, cancer research, and clinical diagnostics.[92]

It has been shown that a device with an on-chip pneumatic microstructure that enables microfluidic control can identify blood types (A, B, and O). With just a fingertip touch, a vacuum activation chamber in this system turns on and off the pressure release section. Point-of-care diagnostic kits for use at home, multiplex assays in biological laboratories, and point-of-care clinical diagnostics in settings with limited resources are all possible applications for this technology.[93]

A microfluidic chip with two valves for sorting and printing cells according to size is described in the technique. Less than d1 cells are eliminated, between d1 and d2 cells are sent to a well plate for printing, and more than d2 cells are destroyed. The method offers a wide range of possibilities for single-cell investigations by dynamically selecting and printing single cells using pressures that may be adjusted. This work indicates that it has numerous potential uses in the realm of single-cell research.[94]

3.2. Materials and Methods

3.2.1. Design of the Pneumatic Valves

First, pneumatic valves of different sizes were fabricated on a two-layer PDMS chip consisting of fluidic and control channels to determine the optimum thickness of the valves. The control channels are located on the top layer, while the fluidic channels are on the bottom layer. Pressure is added to the channel of control. When liquid-filled control channel air pressure is added, the flexible thin PDMS membrane of the control channel, which overlaps at the fluidic channel's top, breaks down and obstructs the flow in the fluidic channel (Figure 3.3).

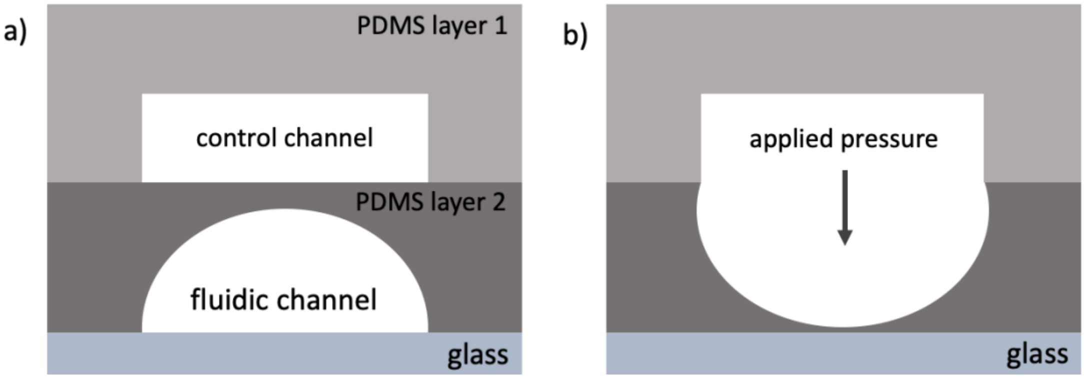

Figure 3.3. The operating principle of the pneumatic microfluidic valve structure. (a) When no pressure is applied to the control channel, the fluidic channel remains open, allowing fluid passage. (b) When pressurized air is applied to the control channel, pressure is exerted on the PDMS membrane between the control channel and the fluidic channel, causing the fluidic channel to close and preventing flow.

The molds designed to produce PDMS layers containing the control and fluidic channels were printed using a 3D printing method capable of printing with 25 µm resolution (Formlabs Form 3, High TempV2). Channels with widths of 200, 400, and 800 µm and a height of 150 µm were printed on separate molds for both control and fluidic channels. The molds obtained after printing were cured at 80°C for 120 minutes. Then, PDMS was prepared at a 1:10 mixing ratio and degassed using a desiccator. For the molds where the control channels were fabricated, PDMS was poured to a height of 2 mm. For the fluidic channels, to obtain a 215 µm thick PDMS layer, PDMS was poured onto the mold and spin-coated at 500 rpm for 30 seconds. The molds coated with PDMS were then cured at 100°C for 1 hour. The cured PDMS layers were removed from the molds, and 15-gauge needles (inner diameter = 1.372 mm, outer diameter = 1.829 mm) were used to create inlet/outlet holes. To bond and attach the layers containing the control and fluidic channels, air plasma (ZEPTO, Diener) was applied to the relevant surfaces at 100 W and 0.5 Torr for 1 minute, and the two surfaces were bonded together. Thus, a thin PDMS membrane with a thickness of 65 µm was formed between the intersecting control and fluidic channels. Inlet and outlet holes were created using 15-gauge needles at the points corresponding to the fluidic channels on the bonded layers. The obtained two-layer PDMS chip was treated with air plasma under the same parameters to be bonded and attached to a glass slide. As a result, a PDMS chip with control and fluidic channels bonded to a glass slide was fabricated (Figure 3.4). In this way, the PDMS chip operates in a manner where fluids can be controlled with an on/off valve principle by supplying the relevant fluids to the fluidic channel and applying distilled water with nitrogen gas to the control channels at a certain pressure.

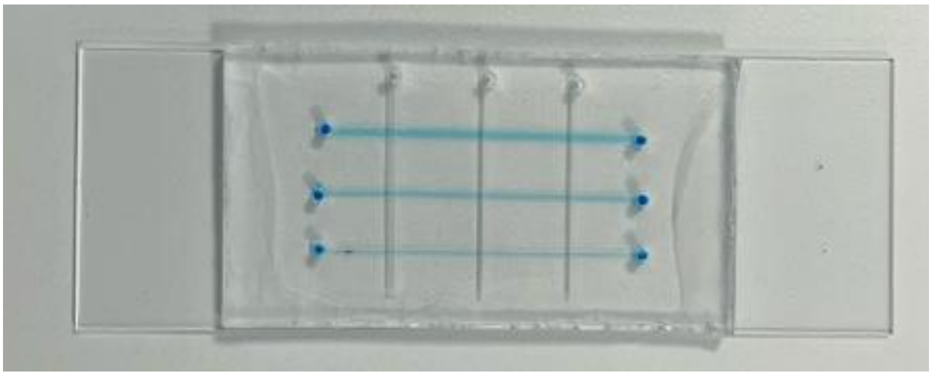

Figure 3.4. View of the chip with pneumatic valve designs. Control and fluidic channels, designed with widths of 200, 400, and 800 µm respectively, are filled with water and a blue-colored solution.

Corresponding to the designed channel molds with widths of 200, 400, and 800 µm, the dimensions obtained after PDMS solidification were measured as 346.031 µm, 489.083 µm, and 887.311 µm for the fluidic channels, and 310 ± 47 µm, 468 ± 60 µm, and 868 ± 64 µm for the control channels (Figure 3.5). This indicates that the resulting molds are slightly wider than the designed molds. The flow has been successfully stopped despite the channel not being perfectly elliptical. The reason for this is the printing accuracy of the 3D printer.

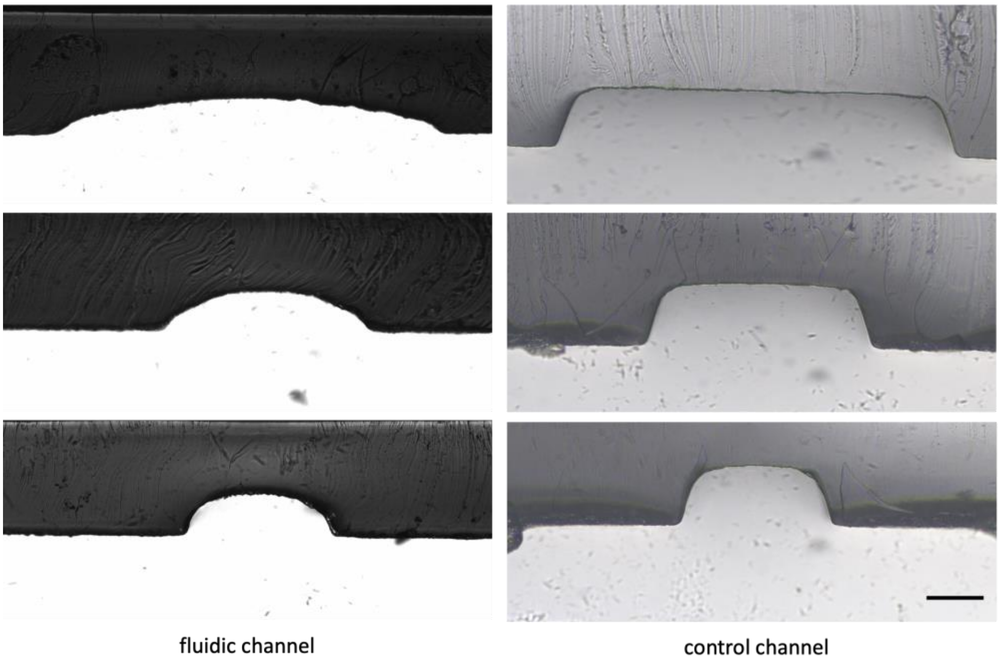

Figure 3.5. The fluidic and control channels' cross-sectional areas from the PDMS layers that were taken out of the molds are displayed in micrographs. Scale Bar: 100 µm.

3.2.2. Design of the Complex Chip

To demonstrate the work on complex microfluidic chip designs, a chip design comprising different chambers was created. In the designed chip, the red channels represent the control channels, while the gray channels denote the fluidic channels (Figure 3.6).

A 3D printer (Formlabs Form 3) was used to build the molds for the fluidic and control channels (Figure 3.7) at a resolution of 0.025 mm using High-Temperature V2 resin. They underwent a post-cure procedure at 80ºC for 120 minutes after being cleaned in isopropyl alcohol for 10 minutes. The microfluidic chip is fabricated in the same way as the chips described in the preceding section. In the fabricated chip, the channels filled with red food dye indicate the control channels, while the channels filled with blue food dye represent the fluidic channels (Figure 3.8).

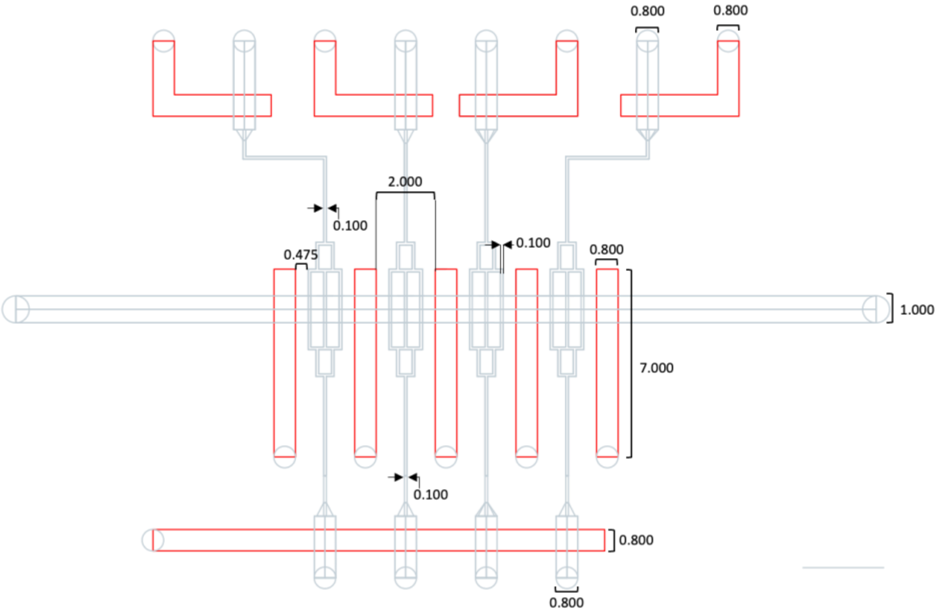

Figure 3.6. Design of a valve microfluidic chip. Red channels represent control channels, grey channels represent fluidic channels, and the circles indicate the inlets and outlets of the channels. Length dimensions are in millimeters. Scale Bar: 3 mm.

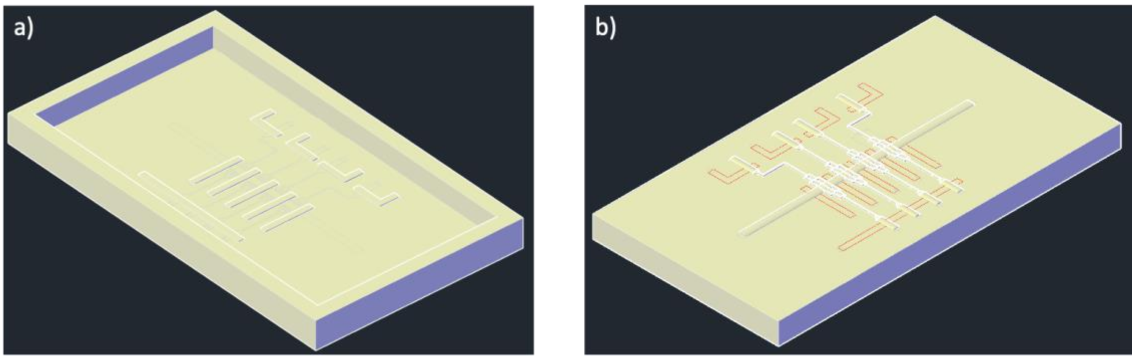

Figure 3.7. 3D images of the molds of (a) the control channel, and (b) the fluidic channel.

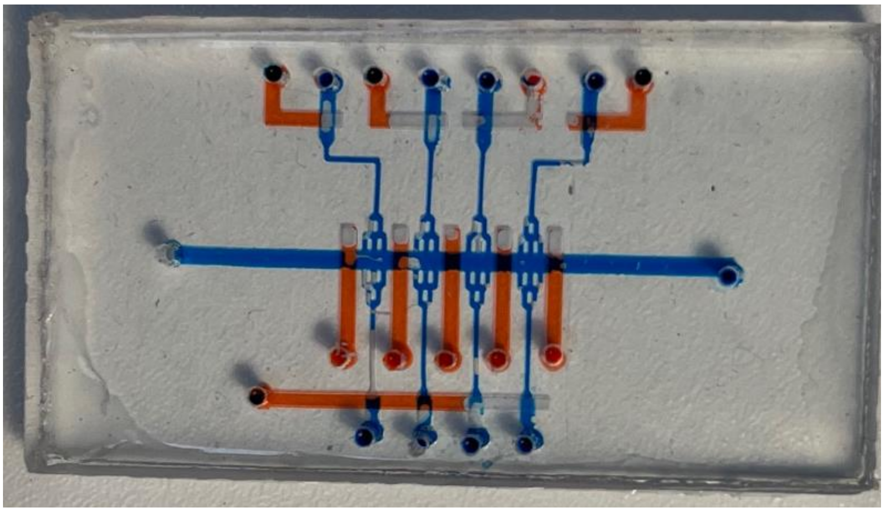

Figure 3.8. Photograph of the microfluidic chip. Blue colored channels indicate fluidic channels and red colored channels indicate control channels.

3.2.3. The Valve Control Setup

The solenoid valves used for valve control are managed by an electronic circuit connected to a microcontroller. The schematic diagram of the electronic circuit capable of controlling five valves is shown in Figure 3.9. In this context, the solenoid valves (MHP1-M4H-3/2G-M3-HC, Festo, Germany) are controlled by commands sent from an Arduino Mega (Arduino Mega 2560 Rev3, Arduino, Italy) microcontroller via MOSFET components (IRF520, International Rectifier, USA).

A circuit capable of controlling five solenoid valves has been fabricated according to the designed circuit schematic (Figure 3.10). The solenoid valves are supplied with gas using pneumatic hoses with an inner diameter of 0.75 mm for gas supply and exhaust. Transfer hoses with an inner diameter of 0.51 mm, connected to the pneumatic hoses, allow nitrogen gas to be delivered at desired pressures to the valve control channels on the microfluidic chip.

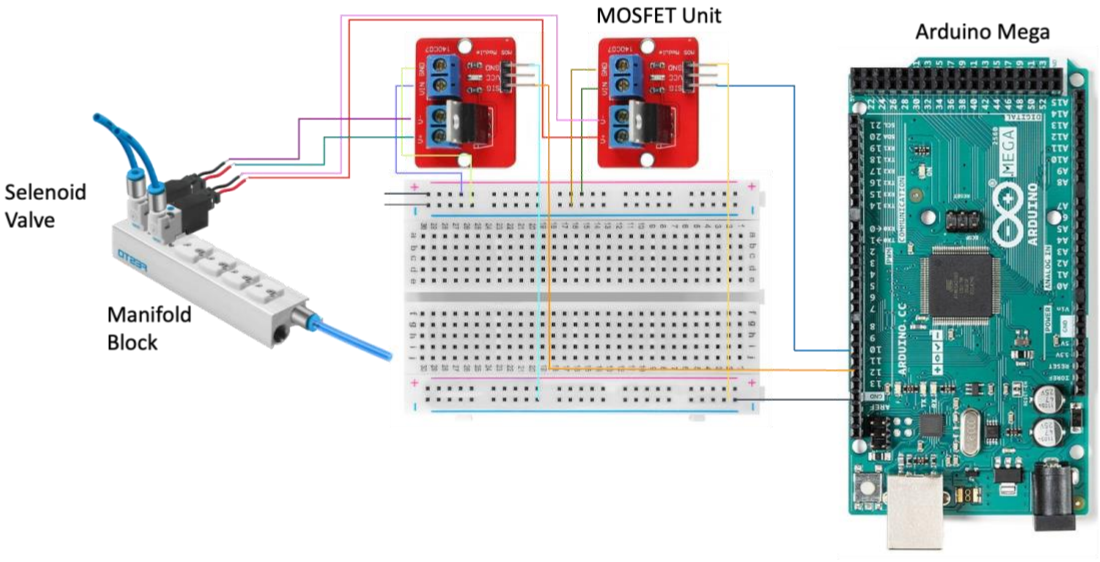

Figure 3.9. Electronic control circuit design for control of solenoid valves.

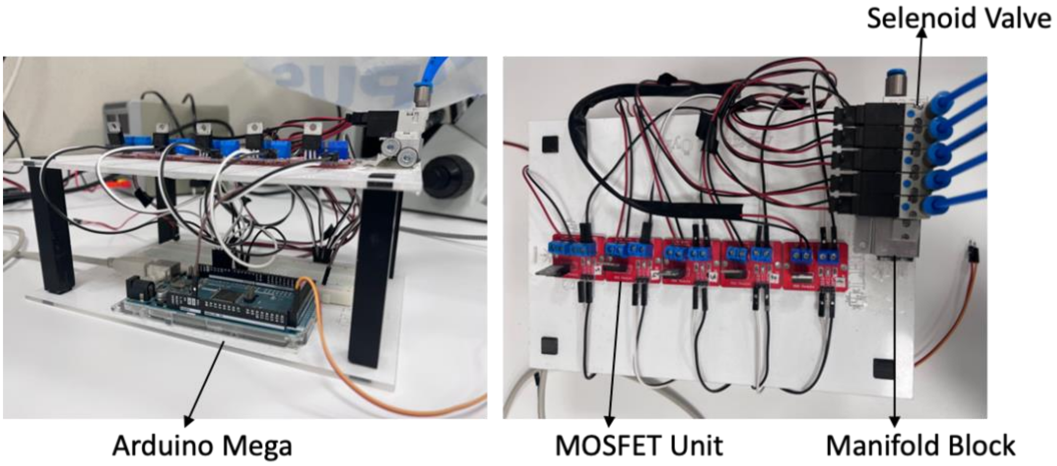

Figure 3.10. Photographs of the designed circuit diagram from different angles.

3.3. Results

3.3.1. Optimization of Valves

Leak tightness and pressure resistance were tested in various width combinations for the channels intended to serve as valves. Channel width combinations of 200, 400, and 800 µm for the control and fluidic channels were investigated to test the leakage and valve functionality. This was accomplished using distilled water in the control channels that were pressurized to 1.5 bar using nitrogen gas, without the use of flow, and by adding food coloring to the fluidic channel (Figure 3.11). It was observed that there was no flow transfer from one area of the fluidic channel to another in the combinations where the fluidic channel was 800 µm wide and the control channels were 400 µm and 800 µm wide. Instead, the control channel worked as a valve, effectively closing the fluidic channel.

For the pressure tests to determine the capability of the control channels to act as valves, blue food dye was introduced at a flow rate of 0.5 mL/h through the 800 µm wide fluidic channel, and the ability of the 400 and 800 µm wide control channels to function as valves was observed under pressures of 0.5, 1, 1.5, and 2 bar (Figure 3.12). These pressure values were chosen to be below the PDMS bonding strength of 4 bar to prevent damage to the PDMS structure. The experiments showed that the 800 µm wide control channels could close the fluidic channel at 1.5 bar, while the 400 µm wide control channels could close it at 2 bar. The stated pressure levels are less than the 4 bar PDMS bonding strength that has been reported in the literature.[95]

Additionally, with an open/close time of 0.02 seconds under a pressure of 2 bar for valve control, the channels can be opened and closed instantaneously (Figure 3.13). This demonstrates that the valve components designed on the microfluidic chip can be used to controllably prevent the passage of fluids from one region of the channel to another.

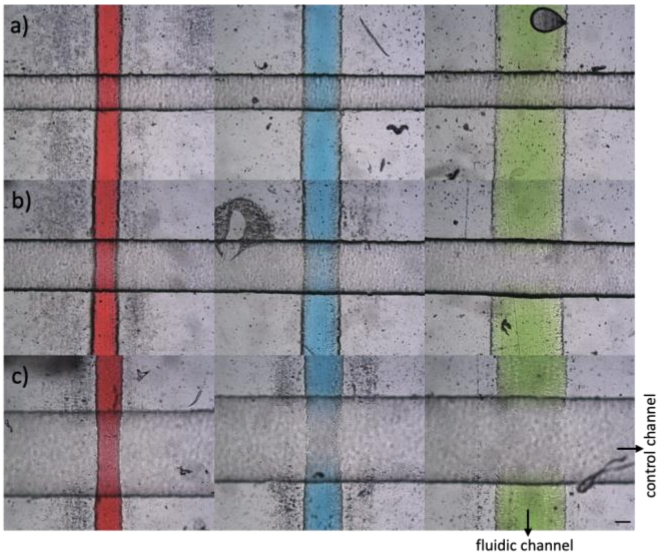

Figure 3.11. Valve characteristics testing of different control and fluidic channels. Red, blue, and green channels indicate 200 µm, 400 µm, and 800 µm fluidic channels respectively. (a) 200 µm, (b) 400 µm and (c) 800 µm transparent channels indicate control channels at 1.5 bar of pressure. Food dye was diluted and put in the fluidic channels, while distilled water was used in the control channels. Scale Bar: 200 µm.

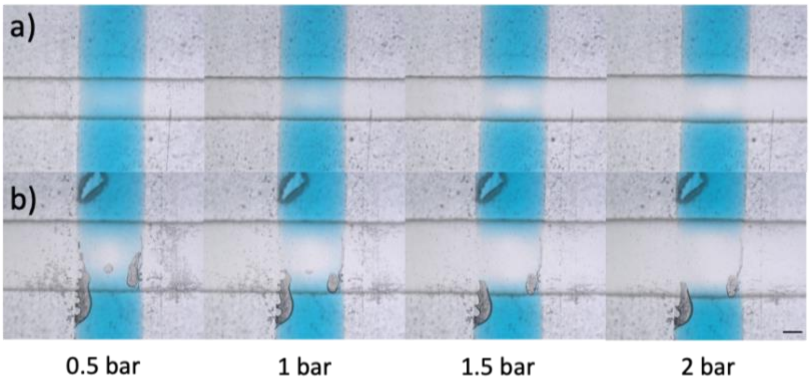

Figure 3.12. Valve properties testing of different control channels underflow. The valve characteristics of the control channels were tested by applying pressures of 0.5, 1, 1.5, and 2 bar to the control channels with widths of (a) 400 µm and (b) 800 µm, while blue food dye was introduced into the fluidic channels at a rate of 0.5 mL/h. Scale Bar: 200 µm.

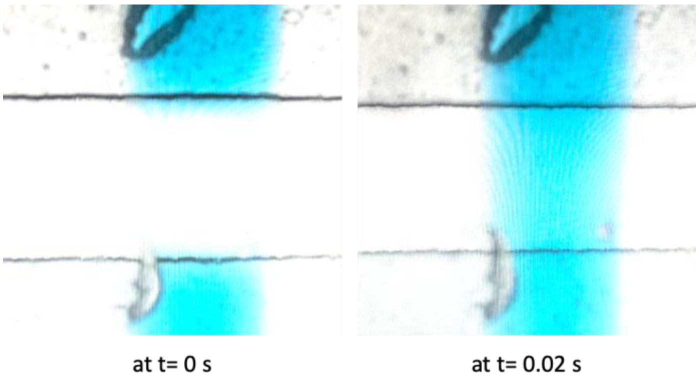

Figure 3.13. The opening and closing times of control channels were tested under 2 bar pressure. According to the measurements, it was observed that valve structures could be opened in 0.02 seconds.

3.3.2. Leakage Tests

On the generated microfluidic chip, flow and pressure-dependent leakage tests of the valves were carried out at various flow and pressure levels. The distilled water was diluted 3:17 times to yield Hoechst 33342 fluorescent dye (Hoechst 33342 Trihydrochloride, Trihydrate - 10 mg/mL Solution in Water, Thermo Fisher Scientific, USA) was introduced into the channels at various flow rates, and its flow-dependent leakage to other chambers was examined. To achieve this, it was investigated whether the fluorescent dye was added at flow rates of 0.1, 0.2, 0.5, and 1 mL/h into the side chambers via valves that were shut under a pressure of 1 bar. No leakage into other chambers was seen through the chamber's left and right valves at any flow rate (Figure 3.14).

Flow-dependent leakage tests were conducted with pressure-dependent sealing agents at 0.25, 0.5, 1, and 1.5 bars applied to the valves at the maximum flow rate of 1 mL/h. Under pressures of 1 and 1.5 bars, it was found that the fluorescent dye did not leak between the chambers (Figure 3.15). Conversely, in pressure-dependent sealing tests, paint transfer was noted between the chambers under 1 mL/h flow and 0.25 and 0.5 bar pressures. It was noted that the valves failed to effectively close the channels at these pressures, resulting in leakage (Figure 3.16). These analyses have demonstrated that the valves effectively shut off the channels at pressures of one bar and higher, allowing for the release of fluid at various flow rates

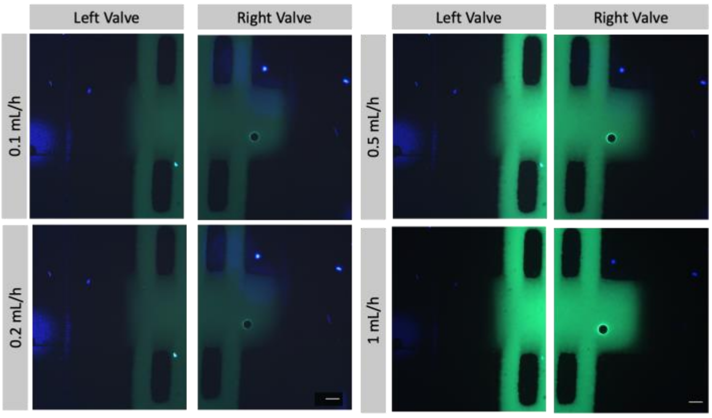

Figure 3.14. The leakage results at different flow rates. Fluorescence microscope images were obtained at 0.1, 0.2, 0.5, and 1 mL/h flow rates from the left and right valves under pressure of 1 bar. It was observed that there was no leakage from underneath the valves, and the fluorescent dye was entirely contained within the chamber. Scale Bar: 200 µm.

.

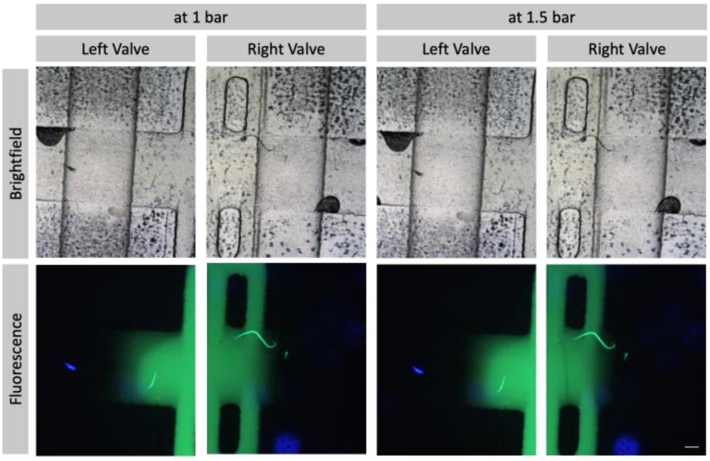

Figure 3.15. The leakage results at 1 and 1.5 bar. Images captured with a brightfield and fluorescence microscope showing the chamber's left and right valves operating at 1 and 1.5 bar of pressure and 1 mL/h of flow. At either pressure value, there was no evidence of chamber leakage. Scale Bar: 200 µm.

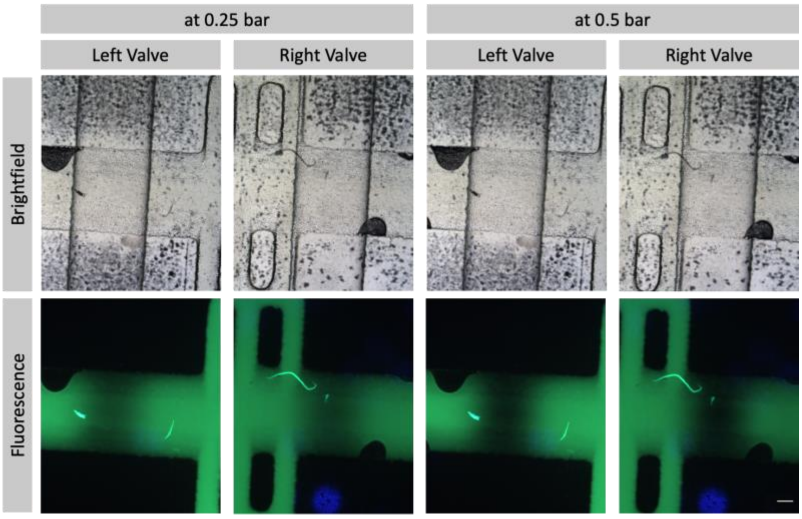

Figure 3.16. The leakage results at 0.25 and 0.5 bar. Images from a brightfield and fluorescence microscope showing the left and right valves of a chamber with a flow rate of 1 mL/h and pressures of 0.25 and 0.5 bar. There was evidence of leakage between the chambers at both pressure levels. Scale Bar: 200 µm.

3.4. Conclusion

The fabrication of micropneumatic valves with molds using 3D printing was observed with different configurations of fluidic and control channels of 200, 400, and 800 µm widths. Under static conditions, it was observed that channels with widths of 400 and 800 µm functioned, and valve closure was observed as the channel width increased. In experiments conducted under flow conditions, valve closure was observed at 1.5 bar and 2 bar in the 800 µm wide fluidic and control channels. Moreover, valve closure occurred at 2 bar in the setup of fluidic and control channels, where the widths were 400 µm and 800 µm, respectively. Upon pressure release, the valve opened in approximately 0.02 seconds, demonstrating the capability for rapid flow control in microfluidics. The configuration of 800 µm wide fluidic and control channels was shown to work in complex microfluidic chip designs. Leakage tests conducted at different flows and pressures were successfully completed. As a result, a rapid, easy, and cost-effective valve design was achieved using the 3D printing method eliminating the requirement for costly, intricate, and labor-intensive production methods. With these advantages, its more widespread use in microfluidic chips is anticipated.

CHAPTER 4

CONCLUSION

The purpose of this thesis is to create a novel image-based cytometry method that measures the density of microparticles under flow conditions inside a microfluidic chip that is placed on a magnetic levitation platform by using deep learning for analysis. In this context, the magnetic levitation platform and microfluidic chip were successfully fabricated. Experiments with beads of varying densities demonstrated that a 5-minute duration with a determined flow rate of 0.05 mL/h was sufficient for the beads to reach equilibrium. Training the YOLOv8 model resulted in high precision and recall values (0.973 and 0.957, respectively). The automatic analysis of levitation height and radius using Python code showed a high correlation with manual results (R^2 values of 0.9987 and 0.9066). It was demonstrated that flow rate is a significant criterion for the successful detection of beads. Detection was achievable at flow rates of 0.05 and 0.1 mL/h, but not at higher rates (0.5 and 1 mL/h). As a result, the flow rate has been a limiting factor during the detection phase. The model trained with the MDA-MB-231 dataset exhibited high precision and recall values. Experiments with U937 cell lines showed the model's effectiveness in distinguishing live and dead cells. This approach enables real-time, label-free detection of micro-particles and cells. To enhance precision and recall values and improve the model's performance, the dataset can be augmented. The dataset initially contained only live cell images. By adding dead cell images, the detection of dead cells can be increased. Additionally, detected microparticles and cells were assigned unique IDs. As a result of repeated detection, the ID of microparticles and cells sometimes increased. This problem has been a limiting factor in the analysis phase.

Moreover, microvalves were studied to sort beads/cells after detection. For this purpose, PDMS-based pneumatic valve production using 3D printing molds was investigated. Valve closure was observed at 1.5 and 2 bar in 800 µm wide channels, and 2 bar in 400 µm and 800 µm control channels. The valve took about 0.02 seconds to open when the pressure was released, allowing for rapid manipulation in microfluidic chips.

Furthermore, successful integration into complex chip designs and successful sealing tests at different flows and pressures demonstrated the effective functioning of pneumatic valves. As a result, a rapid, easy, and cost-effective valve design was achieved using 3D printing without the need for expensive and complex production techniques like photolithography.

By combining pneumatic valve flow control with image and magnetic-based flow cytometry, real-time, label-free, and easy micro-particle and cell sorting can be achieved. The successful integration of magnetic levitation and microfluidics with high-precision machine learning models paves the way for innovative applications in biomedical diagnostics and cell separation. Future work could focus on scaling this technology for high-throughput applications and exploring its potential to detect a broader range of biological entities.

REFERENCES

1. Robinson, J. P. Flow Cytometry: Past and Future. *Biotechniques* **2022**, *72* (4), 159–169. https://doi.org/10.2144/btn-2022-0005.

2. Chantzoura, E.; Kaji, K. Flow Cytometry. In *Basic Science Methods for Clinical Researchers*; Elsevier, 2017; pp 173–189. https://doi.org/10.1016/B978-0-12-803077-6.00010-2.

3. Fleisher, T. A.; Oliveira, J. B. Flow Cytometry. In *Clinical Immunology*; Elsevier, 2019; pp 1239-1251.e1. https://doi.org/10.1016/B978-0-7020-6896-6.00092-2.

4. Adan, A.; Alizada, G.; Kiraz, Y.; Baran, Y.; Nalbant, A. Flow Cytometry: Basic Principles and Applications. *Crit Rev Biotechnol* **2017**, *37* (2), 163–176. https://doi.org/10.3109/07388551.2015.1128876.

5. Montante, S.; Brinkman, R. R. Flow Cytometry Data Analysis: Recent Tools and Algorithms. *Int J Lab Hematol* **2019**, *41* (S1), 56–62. https://doi.org/10.1111/ijlh.13016.

6. Daguerre, H.; Solsona, M.; Cottet, J.; Gauthier, M.; Renaud, P.; Bolopion, A. Positional Dependence of Particles and Cells in Microfluidic Electrical Impedance Flow Cytometry: Origin, Challenges and Opportunities. *Lab Chip* **2020**, *20* (20), 3665–3689. https://doi.org/10.1039/D0LC00616E.

7. Szalóki, G.; Goda, K. Compensation in Multicolor Flow Cytometry. *Cytometry Part A* **2015**, *87* (11), 982–985. https://doi.org/10.1002/cyto.a.22736.

8. Cheung, K. C.; Di Berardino, M.; Schade-Kampmann, G.; Hebeisen, M.; Pierzchalski, A.; Bocsi, J.; Mittag, A.; Tárnok, A. Microfluidic Impedance-based Flow Cytometry. *Cytometry Part A* **2010**, *77A* (7), 648–666. https://doi.org/10.1002/cyto.a.20910.

9. Chen, J.; Xue, C.; Zhao, Y.; Chen, D.; Wu, M.-H.; Wang, J. Microfluidic Impedance Flow Cytometry Enabling High-Throughput Single-Cell Electrical Property Characterization. *Int J Mol Sci* **2015**, *16* (5), 9804–9830. https://doi.org/10.3390/ijms16059804.

10. Graham, M. Don. The Coulter Principle: A History. *Cytometry Part A* **2022**, *101* (1), 8–11. https://doi.org/10.1002/cyto.a.24505.

11. Heidmann, I.; Schade-Kampmann, G.; Lambalk, J.; Ottiger, M.; Di Berardino, M. Impedance Flow Cytometry: A Novel Technique in Pollen Analysis. *PLoS One* **2016**, *11* (11), e0165531. https://doi.org/10.1371/journal.pone.0165531.

12. Song, H.; Wang, Y.; Rosano, J. M.; Prabhakarpandian, B.; Garson, C.; Pant, K.; Lai, E. A Microfluidic Impedance Flow Cytometer for Identification of Differentiation State of Stem Cells. *Lab Chip* **2013**, *13* (12), 2300. https://doi.org/10.1039/c3lc41321g.

13. Clausen, C. H.; Dimaki, M.; Bertelsen, C. V.; Skands, G. E.; Rodriguez-Trujillo, R.; Thomsen, J. D.; Svendsen, W. E. Bacteria Detection and Differentiation Using Impedance Flow Cytometry. *Sensors* **2018**, *18* (10), 3496. https://doi.org/10.3390/s18103496.

14. Voronin, D. V.; Kozlova, A. A.; Verkhovskii, R. A.; Ermakov, A. V.; Makarkin, M. A.; Inozemtseva, O. A.; Bratashov, D. N. Detection of Rare Objects by Flow Cytometry: Imaging, Cell Sorting, and Deep Learning Approaches. *Int J Mol Sci* **2020**, *21* (7), 2323. https://doi.org/10.3390/ijms21072323.

15. Anil-Inevi, M.; Delikoyun, K.; Mese, G.; Tekin, H. C.; Ozcivici, E. Magnetic Levitation Assisted Biofabrication, Culture, and Manipulation of 3D Cellular Structures Using a Ring Magnet Based Setup. *Biotechnol Bioeng* **2021**, *118* (12), 4771–4785. https://doi.org/10.1002/bit.27941.

16. Karakuzu, B.; Anil İnevi, M.; Tarim, E. A.; Sarigil, O.; Guzelgulgen, M.; Kecili, S.; Cesmeli, S.; Koc, S.; Baslar, M. S.; Oksel Karakus, C.; Ozcivici, E.; Tekin, H. C. Magnetic Levitation-Based Miniaturized Technologies for Advanced Diagnostics. *Emergent Mater* **2024**. https://doi.org/10.1007/s42247-024-00762-6.

17. Yenilmez, B.; Knowlton, S.; Tasoglu, S. Self-Contained Handheld Magnetic Platform for Point of Care Cytometry in Biological Samples. *Adv Mater Technol* **2016**, *1* (9). https://doi.org/10.1002/admt.201600144.

18. Alseed, M. M.; Rahmani Dabbagh, S.; Zhao, P.; Ozcan, O.; Tasoglu, S. Portable Magnetic Levitation Technologies. *Advanced Optical Technologies* **2021**, *10* (2), 109–121. https://doi.org/10.1515/aot-2021-0010.

19. Dabbagh, S. R.; Alseed, M. M.; Saadat, M.; Sitti, M.; Tasoglu, S. Biomedical Applications of Magnetic Levitation. *Adv Nanobiomed Res* **2022**, *2* (3). https://doi.org/10.1002/anbr.202100103.

20. Tasoglu, S.; Khoory, J. A.; Tekin, H. C.; Thomas, C.; Karnoub, A. E.; Ghiran, I. C.; Demirci, U. Levitational Image Cytometry with Temporal Resolution. *Advanced Materials* **2015**, *27* (26), 3901–3908. https://doi.org/10.1002/adma.201405660.

21. Chin, E. K.; Grant, C. A.; Giray Ogut, M.; Cai, B.; Gozde Durmus, N. CelLEVITAS: LABEL-FREE RAPID SORTING AND ENRICHMENT OF LIVE CELLS VIA MAGNETIC LEVITATION. https://doi.org/10.1101/2020.07.27.223917.

22. Baday, M.; Calamak, S.; Durmus, N. G.; Davis, R. W.; Steinmetz, L. M.; Demirci, U. Integrating Cell Phone Imaging with Magnetic Levitation (I-LEV) for Label-Free Blood Analysis at the Point-of-Living. *Small* **2016**, *12* (9), 1222–1229. https://doi.org/10.1002/smll.201501845.

23. Luo, S.; Shi, Y.; Chin, L. K.; Hutchinson, P. E.; Zhang, Y.; Chierchia, G.; Talbot, H.; Jiang, X.; Bourouina, T.; Liu, A.-Q. Machine-Learning-Assisted Intelligent Imaging Flow Cytometry: A Review. *Advanced Intelligent Systems* **2021**, *3* (11). https://doi.org/10.1002/aisy.202100073.

24. Luo, S.; Shi, Y.; Chin, L. K.; Hutchinson, P. E.; Zhang, Y.; Chierchia, G.; Talbot, H.; Jiang, X.; Bourouina, T.; Liu, A.-Q. Machine-Learning-Assisted Intelligent Imaging Flow Cytometry: A Review. *Advanced Intelligent Systems* **2021**, *3* (11). https://doi.org/10.1002/aisy.202100073.

25. Nitta, N.; Sugimura, T.; Isozaki, A.; Mikami, H.; Hiraki, K.; Sakuma, S.; Iino, T.; Arai, F.; Endo, T.; Fujiwaki, Y.; Fukuzawa, H.; Hase, M.; Hayakawa, T.; Hiramatsu, K.; Hoshino, Y.; Inaba, M.; Ito, T.; Karakawa, H.; Kasai, Y.; Koizumi, K.; Lee, S.; Lei, C.; Li, M.; Maeno, T.; Matsusaka, S.; Murakami, D.; Nakagawa, A.; Oguchi, Y.; Oikawa, M.; Ota, T.; Shiba, K.; Shintaku, H.; Shirasaki, Y.; Suga, K.; Suzuki, Y.; Suzuki, N.; Tanaka, Y.; Tezuka, H.; Toyokawa, C.; Yalikun, Y.; Yamada, M.; Yamagishi, M.; Yamano, T.; Yasumoto, A.; Yatomi, Y.; Yazawa, M.; Di Carlo, D.; Hosokawa, Y.; Uemura, S.; Ozeki, Y.; Goda, K. Intelligent Image-Activated Cell Sorting. *Cell* **2018**, *175* (1), 266-276.e13. https://doi.org/10.1016/j.cell.2018.08.028.

26. Voronin, D. V.; Kozlova, A. A.; Verkhovskii, R. A.; Ermakov, A. V.; Makarkin, M. A.; Inozemtseva, O. A.; Bratashov, D. N. Detection of Rare Objects by Flow Cytometry: Imaging, Cell Sorting, and Deep Learning Approaches. *Int J Mol Sci* **2020**, *21* (7), 2323. https://doi.org/10.3390/ijms21072323.

27. Huang, K.; Matsumura, H.; Zhao, Y.; Herbig, M.; Yuan, D.; Mineharu, Y.; Harmon, J.; Findinier, J.; Yamagishi, M.; Ohnuki, S.; Nitta, N.; Grossman, A. R.; Ohya, Y.; Mikami, H.; Isozaki, A.; Goda, K. Deep Imaging Flow Cytometry. *Lab Chip* **2022**, *22* (5), 876–889. https://doi.org/10.1039/D1LC01043C.

28. Simonnet, C.; Groisman, A. High-Throughput and High-Resolution Flow Cytometry in Molded Microfluidic Devices. *Anal Chem* **2006**, *78* (16), 5653–5663. https://doi.org/10.1021/ac060340o.

29. Stavrakis, S.; Holzner, G.; Choo, J.; deMello, A. High-Throughput Microfluidic Imaging Flow Cytometry. *Curr Opin Biotechnol* **2019**, *55*, 36–43. https://doi.org/10.1016/j.copbio.2018.08.002.

30. Gao, Q.-H.; Wen, B.; Kang, Y.; Zhang, W.-M. Pump-Free Microfluidic Magnetic Levitation Approach for Density-Based Cell Characterization. *Biosens Bioelectron* **2022**, *204*, 114052. https://doi.org/10.1016/j.bios.2022.114052.

31. Helm, J. M.; Swiergosz, A. M.; Haeberle, H. S.; Karnuta, J. M.; Schaffer, J. L.; Krebs, V. E.; Spitzer, A. I.; Ramkumar, P. N. Machine Learning and Artificial Intelligence: Definitions, Applications, and Future Directions. *Curr Rev Musculoskelet Med* **2020**, *13* (1), 69–76. https://doi.org/10.1007/s12178-020-09600-8.

32. Sarker, I. H. Machine Learning: Algorithms, Real-World Applications and Research Directions. *SN Comput Sci* **2021**, *2* (3), 160. https://doi.org/10.1007/s42979-021-00592-x.

33. Kersting, K. Machine Learning and Artificial Intelligence: Two Fellow Travelers on the Quest for Intelligent Behavior in Machines. *Front Big Data* **2018**, *1*. https://doi.org/10.3389/fdata.2018.00006.

34. Sarker, I. H. Machine Learning: Algorithms, Real-World Applications and Research Directions. *SN Comput Sci* **2021**, *2* (3), 160. https://doi.org/10.1007/s42979-021-00592-x.

35. Jakhar, D.; Kaur, I. Artificial Intelligence, Machine Learning and Deep Learning: Definitions and Differences. *Clin Exp Dermatol* **2020**, *45* (1), 131–132. https://doi.org/10.1111/ced.14029.

36. Hao, X.; Zhang, G.; Ma, S. Deep Learning. *Int J Semant Comput* **2016**, *10* (03), 417–439. https://doi.org/10.1142/S1793351X16500045.

37. Chai, J.; Zeng, H.; Li, A.; Ngai, E. W. T. Deep Learning in Computer Vision: A Critical Review of Emerging Techniques and Application Scenarios. *Machine Learning with Applications* **2021**, *6*, 100134. https://doi.org/10.1016/j.mlwa.2021.100134.

38. Voulodimos, A.; Doulamis, N.; Doulamis, A.; Protopapadakis, E. Deep Learning for Computer Vision: A Brief Review. *Comput Intell Neurosci* **2018**, *2018*, 1–13. https://doi.org/10.1155/2018/7068349.

39. Li, Z.; Dong, M.; Wen, S.; Hu, X.; Zhou, P.; Zeng, Z. CLU-CNNs: Object Detection for Medical Images. *Neurocomputing* **2019**, *350*, 53–59. https://doi.org/10.1016/j.neucom.2019.04.028.

40. Yang, R.; Yu, Y. Artificial Convolutional Neural Network in Object Detection and Semantic Segmentation for Medical Imaging Analysis. *Front Oncol* **2021**, *11*. https://doi.org/10.3389/fonc.2021.638182.

41. Hermessi, H.; Mourali, O.; Zagrouba, E. Convolutional Neural Network-Based Multimodal Image Fusion via Similarity Learning in the Shearlet Domain. *Neural Comput Appl* **2018**, *30* (7), 2029–2045. https://doi.org/10.1007/s00521-018-3441-1.

42. Tulasi Krishna, S. *Deep Learning and Transfer Learning Approaches for Image Classification*; 2019. https://www.researchgate.net/publication/333666150.

43. Wang, P.; Fan, E.; Wang, P. Comparative Analysis of Image Classification Algorithms Based on Traditional Machine Learning and Deep Learning. *Pattern Recognit Lett* **2021**, *141*, 61–67. https://doi.org/10.1016/j.patrec.2020.07.042.

44. Bezdan, T.; Bačanin Džakula, N. Convolutional Neural Network Layers and Architectures. In *Proceedings of the International Scientific Conference - Sinteza 2019*; Singidunum University: Novi Sad, Serbia, 2019; pp 445–451. https://doi.org/10.15308/Sinteza-2019-445-451.

45. Bhatt, D.; Patel, C.; Talsania, H.; Patel, J.; Vaghela, R.; Pandya, S.; Modi, K.; Ghayvat, H. Cnn Variants for Computer Vision: History, Architecture, Application, Challenges and Future Scope. *Electronics (Switzerland)*. MDPI October 1, 2021. https://doi.org/10.3390/electronics10202470.

46. Zafar, A.; Aamir, M.; Mohd Nawi, N.; Arshad, A.; Riaz, S.; Alruban, A.; Dutta, A. K.; Almotairi, S. A Comparison of Pooling Methods for Convolutional Neural Networks. *Applied Sciences* **2022**, *12* (17), 8643. https://doi.org/10.3390/app12178643.

47. Akhtar, N.; Ragavendran, U. Interpretation of Intelligence in CNN-Pooling Processes: A Methodological Survey. *Neural Comput Appl* **2020**, *32* (3), 879–898. https://doi.org/10.1007/s00521-019-04296-5.

48. Alzubaidi, L.; Zhang, J.; Humaidi, A. J.; Al-Dujaili, A.; Duan, Y.; Al-Shamma, O.; Santamaría, J.; Fadhel, M. A.; Al-Amidie, M.; Farhan, L. Review of Deep Learning: Concepts, CNN Architectures, Challenges, Applications, Future Directions. *J Big Data* **2021**, *8* (1). https://doi.org/10.1186/s40537-021-00444-8.

49. Ahmad, T.; Ma, Y.; Yahya, M.; Ahmad, B.; Nazir, S.; Haq, A. ul. Object Detection through Modified YOLO Neural Network. *Sci Program* **2020**, *2020*, 1–10. https://doi.org/10.1155/2020/8403262.

50. Fang, W.; Wang, L.; Ren, P. Tinier-YOLO: A Real-Time Object Detection Method for Constrained Environments. *IEEE Access* **2020**, *8*, 1935–1944. https://doi.org/10.1109/ACCESS.2019.2961959.

51. Du, J. Understanding of Object Detection Based on CNN Family and YOLO. *J Phys Conf Ser* **2018**, *1004*, 012029. https://doi.org/10.1088/1742-6596/1004/1/012029.

52. Redmon, J.; Divvala, S.; Girshick, R.; Farhadi, A. *You Only Look Once: Unified, Real-Time Object Detection*. http://pjreddie.com/yolo/.

53. Wong, A.; Famuori, M.; Shafiee, M. J.; Li, F.; Chwyl, B.; Chung, J. YOLO Nano: A Highly Compact You Only Look Once Convolutional Neural Network for Object Detection. In *2019 Fifth Workshop on Energy Efficient Machine Learning and Cognitive Computing - NeurIPS Edition (EMC2-NIPS)*; IEEE, 2019; pp 22–25. https://doi.org/10.1109/EMC2-NIPS53020.2019.00013.

54. Tarim, E. A.; Erimez, B.; Degirmenci, M.; Cumhur Tekin, H. A Wearable Device Integrated with Deep Learning-Based Algorithms for the Analysis of Breath Patterns. *Advanced Intelligent Systems* **2023**, *5* (11). https://doi.org/10.1002/aisy.202300174.

55. Kaur, A.; Singh, Y.; Neeru, N.; Kaur, L.; Singh, A. A Survey on Deep Learning Approaches to Medical Images and a Systematic Look up into Real-Time Object Detection. *Archives of Computational Methods in Engineering* **2022**, *29* (4), 2071–2111. https://doi.org/10.1007/s11831-021-09649-9.

56. Fang, T.; Yuan, P.; Gong, C.; Jiang, Y.; Yu, Y.; Shang, W.; Tian, C.; Ye, A. Fast Label-Free Recognition of NRBCs by Deep-Learning Visual Object Detection and Single-Cell Raman Spectroscopy. *Analyst* **2022**, *147* (9), 1961–1967. https://doi.org/10.1039/D2AN00024E.

57. Moen, E.; Bannon, D.; Kudo, T.; Graf, W.; Covert, M.; Van Valen, D. Deep Learning for Cellular Image Analysis. *Nat Methods* **2019**, *16* (12), 1233–1246. https://doi.org/10.1038/s41592-019-0403-1.

58. Jiang, H.; Li, S.; Liu, W.; Zheng, H.; Liu, J.; Zhang, Y. Geometry-Aware Cell Detection with Deep Learning. *mSystems* **2020**, *5* (1). https://doi.org/10.1128/mSystems.00840-19.

59. Heo, Y. J.; Lee, D.; Kang, J.; Lee, K.; Chung, W. K. Real-Time Image Processing for Microscopy-Based Label-Free Imaging Flow Cytometry in a Microfluidic Chip. *Sci Rep* **2017**, *7* (1), 11651. https://doi.org/10.1038/s41598-017-11534-0.

60. Li, Y.; Mahjoubfar, A.; Chen, C. L.; Niazi, K. R.; Pei, L.; Jalali, B. Deep Cytometry: Deep Learning with Real-Time Inference in Cell Sorting and Flow Cytometry. *Sci Rep* **2019**, *9* (1), 11088. https://doi.org/10.1038/s41598-019-47193-6.

61. Sarigil, O.; Anil-Inevi, M.; Firatligil-Yildirir, B.; Unal, Y. C.; Yalcin-Ozuysal, O.; Mese, G.; Tekin, H. C.; Ozcivici, E. Scaffold-free Biofabrication of Adipocyte Structures with Magnetic Levitation. *Biotechnol Bioeng* **2021**, *118* (3), 1127–1140. https://doi.org/10.1002/bit.27631.

62. Kecili, S.; Kaymaz, S. V.; Ozogul, B.; Tekin, H. C.; Elitas, M. Investigating Influences of Intravenous Fluids on HUVEC and U937 Monocyte Cell Lines Using the Magnetic Levitation Method. *Analyst* **2023**, *148* (22), 5588–5596. https://doi.org/10.1039/D3AN01304A.

63. Delikoyun, K.; Yaman, S.; Yilmaz, E.; Sarigil, O.; Anil-Inevi, M.; Telli, K.; Yalcin-Ozuysal, O.; Ozcivici, E.; Tekin, H. C. HologLev: A Hybrid Magnetic Levitation Platform Integrated with Lensless Holographic Microscopy for Density-Based Cell Analysis. *ACS Sens* **2021**, *6* (6), 2191–2201. https://doi.org/10.1021/acssensors.0c02587.

64. Kecili, S.; Yilmaz, E.; Ozcelik, O. S.; Anil-Inevi, M.; Gunyuz, Z. E.; Yalcin-Ozuysal, O.; Ozcivici, E.; Tekin, H. C. MDACS Platform: A Hybrid Microfluidic Platform Using Magnetic Levitation Technique and Integrating Magnetic, Gravitational, and Drag Forces for Density-Based Rare Cancer Cell Sorting. *Biosens Bioelectron X* **2023**, *15*, 100392. https://doi.org/10.1016/j.biosx.2023.100392.

65. Yaman, S.; Tekin, H. C. Magnetic Susceptibility-Based Protein Detection Using Magnetic Levitation. *Anal Chem* **2020**, *92* (18), 12556–12563. https://doi.org/10.1021/acs.analchem.0c02479.

66. Sarigil, O.; Anil-Inevi, M.; Yilmaz, E.; Mese, G.; Tekin, H. C.; Ozcivici, E. Label-Free Density-Based Detection of Adipocytes of Bone Marrow Origin Using Magnetic Levitation. *Analyst* **2019**, *144* (9), 2942–2953. https://doi.org/10.1039/C8AN02503G.

67. Abe, N.; Institute of Electrical and Electronics Engineers; IEEE Computer Society. *2018 IEEE International Conference on Big Data : Proceedings : Dec 10 - Dec 13, 2018, Seattle, WA, USA.*

68. Vijayakumar, A.; Vairavasundaram, S. YOLO-Based Object Detection Models: A Review and Its Applications. *Multimed Tools Appl* **2024**. https://doi.org/10.1007/s11042-024-18872-y.

69. Du, F.-J.; Jiao, S.-J. Improvement of Lightweight Convolutional Neural Network Model Based on YOLO Algorithm and Its Research in Pavement Defect Detection. *Sensors* **2022**, *22* (9), 3537. https://doi.org/10.3390/s22093537.

70. Sirisha, U.; Praveen, S. P.; Srinivasu, P. N.; Barsocchi, P.; Bhoi, A. K. Statistical Analysis of Design Aspects of Various YOLO-Based Deep Learning Models for Object Detection. *International Journal of Computational Intelligence Systems* **2023**, *16* (1), 126. https://doi.org/10.1007/s44196-023-00302-w.

71. Lee, J.; Hwang, K. YOLO with Adaptive Frame Control for Real-Time Object Detection Applications. *Multimed Tools Appl* **2022**, *81* (25), 36375–36396. https://doi.org/10.1007/s11042-021-11480-0.

72. Pereira, N. PereiraASLNet: ASL Letter Recognition with YOLOX Taking Mean Average Precision and Inference Time Considerations. In *2022 2nd International Conference on Artificial Intelligence and Signal Processing (AISP)*; IEEE, 2022; pp 1–6. https://doi.org/10.1109/AISP53593.2022.9760665.

73. Liu, G.; Nouaze, J. C.; Touko Mbouembe, P. L.; Kim, J. H. YOLO-Tomato: A Robust Algorithm for Tomato Detection Based on YOLOv3. *Sensors* **2020**, *20* (7), 2145. https://doi.org/10.3390/s20072145.

74. Sackmann, E. K.; Fulton, A. L.; Beebe, D. J. The Present and Future Role of Microfluidics in Biomedical Research. *Nature* **2014**, *507* (7491), 181–189. https://doi.org/10.1038/nature13118.

75. Yang, Y.; Chen, Y.; Tang, H.; Zong, N.; Jiang, X. Microfluidics for Biomedical Analysis. *Small Methods* **2020**, *4* (4). https://doi.org/10.1002/smtd.201900451.

76. Mu, X.; Zheng, W.; Sun, J.; Zhang, W.; Jiang, X. Microfluidics for Manipulating Cells. *Small* **2013**, *9* (1), 9–21. https://doi.org/10.1002/smll.201200996.

77. Ren, K.; Chen, Y.; Wu, H. New Materials for Microfluidics in Biology. *Curr Opin Biotechnol* **2014**, *25*, 78–85. https://doi.org/10.1016/j.copbio.2013.09.004.

78. Weisgrab, G.; Ovsianikov, A.; Costa, P. F. Functional 3D Printing for Microfluidic Chips. *Adv Mater Technol* **2019**, *4* (10). https://doi.org/10.1002/admt.201900275.

79. Gong, H.; Woolley, A. T.; Nordin, G. P. High Density 3D Printed Microfluidic Valves, Pumps, and Multiplexers. *Lab Chip* **2016**, *16* (13), 2450–2458. https://doi.org/10.1039/C6LC00565A.

80. Tzivelekis, C.; Sgardelis, P.; Waldron, K.; Whalley, R.; Huo, D.; Dalgarno, K. Fabrication Routes via Projection Stereolithography for 3D-Printing of Microfluidic Geometries for Nucleic Acid Amplification. *PLoS One* **2020**, *15* (10), e0240237. https://doi.org/10.1371/journal.pone.0240237.

81. Huang, J.; Qin, Q.; Wang, J. A Review of Stereolithography: Processes and Systems. *Processes* **2020**, *8* (9), 1138. https://doi.org/10.3390/pr8091138.

82. Huang, S.; He, Q.; Hu, X.; Chen, H. Fabrication of Micro Pneumatic Valves with Double-Layer Elastic Poly(Dimethylsiloxane) Membranes in Rigid Poly(Methyl Methacrylate) Microfluidic Chips. *Journal of Micromechanics and Microengineering* **2012**, *22* (8), 085008. https://doi.org/10.1088/0960-1317/22/8/085008.

83. Mohan, R.; Schudel, B. R.; Desai, A. V.; Yearsley, J. D.; Apblett, C. A.; Kenis, P. J. A. Design Considerations for Elastomeric Normally Closed Microfluidic Valves. *Sens Actuators B Chem* **2011**, *160* (1), 1216–1223. https://doi.org/10.1016/j.snb.2011.09.051.

84. Chen, C.; Li, P.; Guo, T.; Chen, S.; Xu, D.; Chen, H. Generation of Dynamic Concentration Profile Using A Microfluidic Device Integrating Pneumatic Microvalves. *Biosensors (Basel)* **2022**, *12* (10), 868. https://doi.org/10.3390/bios12100868.

85. Lau, A.; Yip, H.; Ng, K.; Cui, X.; Lam, R. Dynamics of Microvalve Operations in Integrated Microfluidics. *Micromachines (Basel)* **2014**, *5* (1), 50–65. https://doi.org/10.3390/mi5010050.

86. Ni, J.; Li, B.; Yang, J. A Pneumatic PDMS Micropump with In-Plane Check Valves for Disposable Microfluidic Systems. *Microelectron Eng* **2012**, *99*, 28–32. https://doi.org/10.1016/j.mee.2012.04.002.

87. Zhou, Y.; Yu, Z.; Wu, M.; Lan, Y.; Jia, C.; Zhao, J. Single-Cell Sorting Using Integrated Pneumatic Valve Droplet Microfluidic Chip. *Talanta* **2023**, *253*, 124044. https://doi.org/10.1016/j.talanta.2022.124044.

88. Oh, C. K.; Lee, S. W.; Jeong, O. C. Fabrication of Pneumatic Valves with Spherical Dome-Shape Fluid Chambers. *Microfluid Nanofluidics* **2015**, *19* (5), 1091–1099. https://doi.org/10.1007/s10404-015-1627-8.

89. Simone, G.; Perozziello, G.; Sardella, G.; Disegna, I.; Tori, S.; Manaresi, N.; Medoro, G. A Microvalve for Hybrid Microfluidic Systems. *Microsystem Technologies* **2010**, *16* (7), 1269–1276. https://doi.org/10.1007/s00542-009-0986-z.

90. Sia, S. K.; Whitesides, G. M. Microfluidic Devices Fabricated in Poly(Dimethylsiloxane) for Biological Studies. *Electrophoresis* **2003**, *24* (21), 3563–3576. https://doi.org/10.1002/elps.200305584.

91. Brower, K.; Puccinelli, R. R.; Markin, C. J.; Shimko, T. C.; Longwell, S. A.; Cruz, B.; Gomez-Sjoberg, R.; Fordyce, P. M. An Open-Source, Programmable Pneumatic Setup for Operation and Automated Control of Single- and Multi-Layer Microfluidic Devices. *HardwareX* **2018**, *3*, 117–134. https://doi.org/10.1016/j.ohx.2017.10.001.

92. Zhao, L.; Ma, C.; Shen, S.; Tian, C.; Xu, J.; Tu, Q.; Li, T.; Wang, Y.; Wang, J. Pneumatic Microfluidics-Based Multiplex Single-Cell Array. *Biosens Bioelectron* **2016**, *78*, 423–430. https://doi.org/10.1016/j.bios.2015.09.055.

93. Chen, A.; Pan, T. Manually Operatable On-Chip Bistable Pneumatic Microstructures for Microfluidic Manipulations. *Lab Chip* **2014**, *14* (17), 3401. https://doi.org/10.1039/C4LC00540F.

94. Chen, C.; Zhu, Y.; Ho, J. W. K.; Chen, H. The Method to Dynamically Screen and Print Single Cells Using Microfluidics with Pneumatic Microvalves. *MethodsX* **2021**, *8*, 101190. https://doi.org/10.1016/j.mex.2020.101190.

95. Kecili, S.; Tekin, H. C. Adhesive Bonding Strategies to Fabricate High-Strength and Transparent 3D Printed Microfluidic Device. *Biomicrofluidics* **2020**, *14* (2). https://doi.org/10.1063/5.0003302.

APPENDIX A

```
from collections import defaultdict
import matplotlib.pyplot as plt
from ultralytics import YOLO
import cv2
model = YOLO("best.pt")
video_path = "example.mov"
cap = cv2.VideoCapture(video_path)
fourcc = cv2.VideoWriter_fourcc(*'mp4v')
fps = 30
frame_width = int(cap.get(cv2.CAP_PROP_FRAME_WIDTH))
frame_size = (frame_width, int(cap.get(cv2.CAP_PROP_FRAME_HEIGHT)))
out = cv2.VideoWriter('output.mp4', fourcc, fps, frame_size)
# Store the track history
track_history = defaultdict(lambda: {'levitation_heights': [], 'detected_particles': []})
magnet_location = 1030
# Loop through the video frames
while cap.isOpened():
    # Read a frame from the video
    success, frame = cap.read()
    if success:
        # Run YOLOv8 tracking on the frame, persisting tracks between frames
        results = model.track(frame, persist=True)
```

```
        # Get the boxes and track IDs
        boxes = results[0].boxes.xywh.cpu()
        # track_ids = results[0].boxes.id.int().cpu().tolist()
        id_value = results[0].boxes.id
        if id_value is not None:
            track_ids = id_value.cpu().tolist()
            for box, track_id in zip(boxes, track_ids):
                x, y, w, h = box
                lev_height = magnet_location - (float(y)+(float(h)/2))
                particle_radius = w / 2
                particle_radius2 = h / 2
                track_history[track_id]['levitation_heights'].append(lev_height)
                track_history[track_id]['detected_particles'].append((particle_radius, particle_radius2))  # Store both radii
        # Visualize the results on the frame
        annotated_frame = results[0].plot()
        avg_levitation_height_per_track = {}
        avg_particle_radius_per_track = {}
        avg_particle_radius2_per_track = {}  # New dictionary for second radius
        for track_id, track_data in track_history.items():
            levitation_heights = track_data['levitation_heights']
            detected_particles = track_data['detected_particles']
            avg_levitation_height_per_track[track_id] = sum(levitation_heights) / len(levitation_heights)
```

```
            avg_particle_radius_per_track[track_id] = sum(p[0] for p in detected_particles) / len(detected_particles)  # Use first radius (width) for calculation
            avg_particle_radius2_per_track[track_id] = sum(p[1] for p in detected_particles) / len(detected_particles)  # Use second radius (height) for calculation
        print("Average Levitation Height per track:", avg_levitation_height_per_track)
        print("Average Particle Radius per track:", avg_particle_radius_per_track)
        print("Average Particle Radius2 per track:", avg_particle_radius2_per_track)
        # Display the annotated frame
        out.write(annotated_frame)
        cv2.imshow("YOLOv8 Tracking", annotated_frame)
        # Break the loop if 'q' is pressed
        if cv2.waitKey(1) & 0xFF == ord("q"):
            break
    else:
        # Break the loop if the end of the video is reached
        break
# Write average levitation and radius values per track to a text file
with open('track_data.txt', 'w') as file:
    file.write("Track ID\tAverage Levitation Height (um)\tAverage Particle Radius (um)\tAverage Particle Radius2 (um)\n")
    for track_id in avg_levitation_height_per_track:
file.write(f"{track_id}\t{avg_levitation_height_per_track[track_id]:.2f}\t{avg_particle_radius_per_track[track_id]:.2f}\t{avg_particle_radius2_per_track[track_id]:.2f}\n")
# Write all levitation and radius values for each track to the text file
for track_id, track_data in track_history.items():
    levitation_heights = track_data['levitation_heights']
```

```
    detected_particles = track_data['detected_particles']

    with open('track_data.txt', 'a') as file:

        file.write(f"\nTrack ID: {track_id}\n")

        file.write("Frame\tLevitation Height (um)\tParticle Radius (um)\tParticle Radius2 (um)\n")

        for i in range(len(levitation_heights)):

            file.write(f"{i + 1}\t{levitation_heights[i]:.2f}\t{detected_particles[i][0]:.2f}\t{detected_particles[i][1]:.2f}\n")  # Write both radii

# Write the average levitation and radius values for all tracks to the text file

with open('track_data.txt', 'a') as file:

    file.write("\nAverage Levitation Height and Particle Radius per Track:\n")

    for track_id in track_history.keys():

        file.write(f"Track ID: {track_id}\n")

        file.write(f"Average Levitation Height: {avg_levitation_height_per_track[track_id]:.2f} um\n")

        file.write(f"Average Particle Radius: {avg_particle_radius_per_track[track_id]:.2f} um\n")

        file.write(f"Average Particle Radius2: {avg_particle_radius2_per_track[track_id]:.2f} um\n\n")

# Plot average levitation height vs. average particle radius for each track

plt.scatter(avg_particle_radius_per_track.values(), avg_levitation_height_per_track.values(), marker='*')

plt.xlabel('Average Particle Radius (um)')

plt.ylabel('Average Levitation Height (um)')

plt.ylim(100, 1000)
```

```
plt.xlim(0,20)

plt.title('Average Levitation Height vs. Average Particle Radius per Track (Radius1)')

plt.grid(True)

plt.savefig('average_levitation_vs_radius1_per_track.png')

plt.show()

# Plot average levitation height vs. average particle radius2 for each track

plt.scatter(avg_particle_radius2_per_track.values(), avg_levitation_height_per_track.values(), marker='*')

plt.xlabel('Average Particle Radius2 (um)')

plt.ylabel('Average Levitation Height (um)')

plt.ylim(100, 1000)

plt.xlim(0,20)

plt.title('Average Levitation Height vs. Average Particle Radius2 per Track (Radius2)')

plt.grid(True)

plt.savefig('average_levitation_vs_radius2_per_track.png')

plt.show()

# Release the video capture object and close the display window

cap.release()

cv2.destroyAllWindows()
```

APPENDIX B

```
import cv2
def mouse_drawing(event, x, y, flags, params):

if event == cv2.EVENT_LBUTTONDOWN: print('(', x, ',', y, ')')
circles.append((x, y))
cv2.circle(image_copy, (x, y), 5, (0, 0, 255), -1) cv2.imshow("Image", image_copy)

def draw_circles_on_image(image): for center_position in circles:

cv2.circle(image, center_position, 5, (0, 0, 255), -1) cv2.imshow("Image", image)

# Load the image
image_path = "mık.tiff"
image = cv2.imread(image_path)
# Check if the image is loaded successfully if image is None:

print("Error: Unable to load the image.")

exit()
cv2.setMouseCallback("Image", mouse_drawing) circles = []
# Draw circles on the image draw_circles_on_image(image)
while True:

key = cv2.waitKey(1) if key == ord("q"):

break
elif key == ord("w"):

circles = []
image_copy = image.copy() draw_circles_on_image(image_copy)
cv2.destroyAllWindows()
```